THE ASTROPHYSICAL JOURNAL, 931:77 (15pp), 2022 June 1 https://doi.org/10.3847/1538-4357/ac6955

Accretion Disk Outflow during the X-Ray Flare of the Super-Eddington Active Nucleus of I Zwicky 1

Yuanze Ding[1,2,3], Ruancun Li[1,4], Luis C. Ho[1,4], and Claudio Ricci[1,5]
[1] Kavli Institute for Astronomy and Astrophysics, Peking University, Beijing 100871, People's Republic of China; liruancun@pku.edu.cn
[2] WHU-NAOC Joint Center for Astronomy, Wuhan University, Wuhan 430072, People's Republic of China
[3] Hongyi Honor College, Wuhan University, Wuhan 430072, People's Republic of China
[4] Department of Astronomy, School of Physics, Peking University, Beijing 100871, People's Republic of China
[5] Núcleo de Astronomía de la Facultad de Ingeniería, Universidad Diego Portales, Av. Ejército Libertador 441, Santiago, Chile
Received 2022 April 5; revised 2022 April 20; accepted 2022 April 20; published 2022 May 26

Abstract

We present a detailed X-ray spectral analysis of the narrow-line Seyfert 1 galaxy I Zwicky 1, for which a sequence of X-ray flares were detected during a long, simultaneous observation acquired with XMM-Newton and NuSTAR. We determine the key parameters of the inner accretion disk and hot corona in the context of the disk reflection model, which successfully captures the evolution of the X-ray corona during the X-ray flare. Using a thermal Comptonization continuum model, we confirm that the corona rapidly cooled from ∼200 to ∼15 keV, likely a consequence of strong pair production and runaway in a disk-like corona during the X-ray flare, when the nonthermal electron fraction rapidly increased. We detect multiple variable blueshifted absorption features arising from outflowing material along the line of sight to I Zwicky 1, which we associated with ionized winds and ultrafast outflows. One of the ionized winds may be newly launched just after the X-ray flare. During the 5 days of NuSTAR observations, the ionization state and velocity of these outflows followed a relation of the form $\xi \sim v_w^{3.24}$, as expected from a super-Eddington wind. Comparison with molecular gas and warm ionized gas observations suggests that the kinematics of the ionized winds are consistent with a sufficiently cooled, momentum-driven outflow. Considering the dynamical feedback from these outflows can account for the significantly undermassive black hole in I Zwicky 1.

Unified Astronomy Thesaurus concepts: Active galaxies (17); Quasars (1319); Black holes (162); Accretion (14)

1. Introduction

The discovery of empirical correlations between supermassive black holes (BHs) and the properties of their host galaxies has raised intensive interest in the role of active galactic nucleus (AGN) feedback in galaxy evolution (Fabian 2012; Kormendy & Ho 2013; Heckman & Best 2014), and references therein). Of the many forms of energy injection emanating from AGNs, one of the most notable are the powerful winds associated with the so-called ultrafast outflows (UFOs; for a review of the theory, see King & Pounds 2015) detected in sources radiating near or above the Eddington limit. These absorbers, characterized by a high-ionization state ($\xi \approx 10^3-10^6$ erg cm s^{-1}) and mildly relativistic velocities (∼$0.03-0.3c$; Vignali et al. 2015; Tombesi 2016; Braito et al. 2018; Pinto et al. 2018; Serafinelli et al. 2019, and references therein), are often detected in the region of 7−9 keV as Fe XXV/XXVI K-shell lines with column density $N_{\rm H} \approx 10^{22}-10^{24}$ cm^{-2}. However, there have been recent detections of UFOs also in the soft X-ray band (e.g., Longinotti et al. 2015; Pounds et al. 2016; Reeves et al. 2016; Sanfrutos et al. 2018; Ricci et al. 2021). The extreme winds are believed to originate from the accretion disk within a hundred gravitational radii from the BH. Due to their relatively wide solid angle ($\Omega/2\pi \simeq 0.4$; Tombesi et al. 2010; Gofford et al. 2015), they can transport a significant amount of kinetic energy from the vicinity of supermassive BHs to their host galaxies. A BH accreting at super-Eddington rates ($\dot{m}_{\rm Edd} \approx 10$–100)[6] can drive outflows with velocities of ∼0.1–0.3c (King & Muldrew 2016). Strong, fast outflows, an intrinsic attribute of super-Eddington accretion (Jiang et al. 2014, 2019), may be an effective agent for quasar-mode feedback (Fabian 2012).

Observations indicate that UFOs are mostly multiphase (Piro et al. 2005; Pounds & King 2013; Sanfrutos et al. 2018, and references therein), in agreement with current models (e.g., King 2003, 2005, 2010a, 2010b; Zubovas & King 2014; King & Muldrew 2016) that predict that outflows from the inner disk shock and transfer kinetic energy to the ambient medium. The absorbing material can be described by four different regions (King 2010a; King & Pounds 2015): (1) the inner UFO region, (2) the shocked UFO region, (3) the shocked, swept-up interstellar medium, and (4) the outer ambient medium, which has not yet been affected by inner outflows.

Another kind of outflowing wind—the warm absorber (WA)—appears in the soft X-ray band. Characterized by lower ionization state ($\xi \lesssim 10^2$ erg cm s^{-1}) and outflow velocity (∼100−1000 km s^{-1}), WAs are often detected in soft X-rays as absorption lines and edges from H-like and He-like ions of C, O, N, Ne, Mg, Al, Si, and S. Mizumoto et al. (2019) identify WAs as a thermal component associated with the torus and/or a wind from the broad-line region. The existence of WAs significantly complicates the study of UFOs, as care must be exercised to distinguish UFO features from absorption lines

[6] The Eddington ratio is defined as $\lambda_{\rm Edd} \equiv L_{\rm bol}/L_{\rm Edd}$, where $L_{\rm bol}$ is the bolometric luminosity, $L_{\rm Edd} = 1.26 \times 10^{38}\,(M_\bullet/M_\odot)$ erg s^{-1} is the Eddington luminosity, and $M_\bullet$ is the BH mass. We define the Eddington mass accretion rate as $\dot{M}_{\rm Edd} \equiv L_{\rm Edd}/c^2\epsilon$ and accretion Eddington ratio $\dot{m}_{\rm Edd} = \dot{M}_\bullet/\dot{M}_{\rm Edd}$, where ϵ is the radiation efficiency at $L_{\rm Edd}$.

produced by the Galactic interstellar medium and WAs. Pounds & King (2013) and Sanfrutos et al. (2018) invoke the framework of a *shocked outflow* to interpret the detection of low-ionization UFOs and variable WAs (e.g., Pinto et al. 2013, 2018; Porquet & Dubau 2000).

The X-ray emission in AGNs mainly originates from a hot corona of relativistic electrons located in the vicinity of the BH (Haardt & Maraschi 1991, 1993). Thermal ultraviolet/optical photons emitted from the accretion disk are inverse-Compton scattered by these hot electrons into the X-rays, creating a power-law continuum with an exponential high-energy cutoff. The parameters of the corona, including the primary power-law photon index Γ, the cutoff energy or electron temperature kT_e, and optical depth, systematically depend on the Eddington ratio and mass of the BH. In their analysis of the AGNs from the Swift/BAT catalog, Ricci et al. (2018) report a clear inverse correlation between the cutoff energy and $\lambda_{\rm Edd}$, while numerous previous studies have confirmed that Γ correlates positively with $\lambda_{\rm Edd}$ (Shemmer et al. 2008; Risaliti et al. 2009; Brightman et al. 2013; Trakhtenbrot et al. 2017), at least in the regime of moderate-to-high $\lambda_{\rm Edd}$ ($\lambda_{\rm Edd} \gtrsim 0.01$; Yang et al. 2015; She et al. 2018).

Broadband X-ray spectroscopy can place more stringent constraints on the geometry and heating and thermalization mechanisms of the corona (Fabian et al. 2015), as well as potentially link them to the physical properties of outflows. This is the goal of this study. We perform a detailed analysis of simultaneous observations with the X-ray Multi-Mirror Mission (XMM-Newton; Jansen et al. 2001) and Nuclear Spectroscopy Telescope Array (NuSTAR; Harrison et al. 2013) of the prototype narrow-line Seyfert 1 galaxy I Zwicky 1 (I Zw 1). Previous XMM-Newton observations of this source have revealed multicomponent, ionized gas consistent with an WA origin, as well as an apparent inverse correlation between X-ray ionization and ionizing luminosity on timescales of years (Costantini et al. 2007). Recent work using the Reflection Grating Spectrometer (RGS) onboard XMM-Newton found changes in the ionization state of the WA that are not correlated straightforwardly with the continuum variability, suggesting shortcomings of classical WA models (Costantini et al. 2007; Silva et al. 2018). It has been argued that the variation of ionization state primarily depends on the density of the clumps, which may arise from an inhomogeneous outflow radiatively driven from the accretion disk (Silva et al. 2018). Absorption troughs at ∼8 and ∼8.5 keV suggest the existence of a fast disk wind (Mizumoto et al. 2019) and a high accretion rate (Jiang et al. 2014), in qualitative agreement with the optical reverberation mapping experiment of Huang et al. (2019), which estimates a super-Eddington accretion rate of $\dot{M} = 203.9^{+61.0}_{-65.8}\, L_{\rm Edd}\, c^{-2}$ onto a BH of mass $M_{\bullet} = 9.30^{+1.26}_{-1.38} \times 10^6\, M_\odot$. The bolometric luminosity of $L_{\rm bol} \approx 3 \times 10^{45}$ erg s^{-1} (by scaling 5100 Å; Porquet et al. 2004) also formally exceeds the Eddington luminosity of 1.17×10^{45} erg s^{-1}. A more recent estimation using CLUMPY to describe the distribution of clouds that form the dusty torus produces generally consistent results, with $L_{\rm bol} = (4.0 \pm 0.3) \times 10^{45}$ erg s^{-1} (Martínez-Paredes et al. 2017).

This work identifies several fast outflows with very different ionization states in I Zw 1. The long NuSTAR and XMM-Newton observations enable us to compare the kinematics of the UFOs with the shock wave models. Using a reflection model to fit the soft X-ray excess and the broad Fe Kα line reveals an inverse correlation between photon index and X-ray luminosity, together with evidence that the X-ray corona rapidly cools on a short timescale. Section 2 describes the data reduction procedures of the X-ray observations. Section 3 presents the spectral fitting. Implications for the properties of the outflows and corona are discussed in Section 4. Main conclusions appear in Section 5. For standard cosmological parameters of $\Omega_\Lambda = 0.73$, $\Omega_m = 0.27$, and $H_0 = 70$ km s^{-1} Mpc^{-1}, the redshift of $z = 0.061169$ for I Zw 1 (Springob et al. 2005) corresponds to a luminosity distance of 274 Mpc.

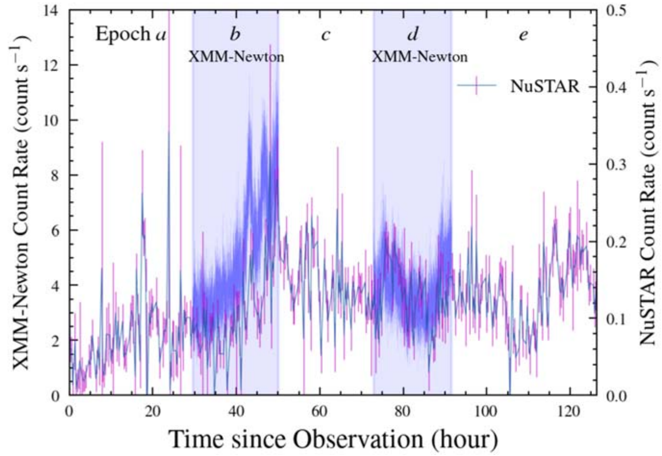

Figure 1. The XMM-Newton (0.2–10 keV) and NuSTAR (3–78 keV) X-ray light curves during the entire ∼5 day duration of the NuSTAR observation. We divide the long observation into five segments (labeled *a*–*e*) in order to investigate the spectral evolution.

2. Observations

Figure 1 provides an overview of the total time span during which I Zw 1 was observed in X-rays. Of the ∼455 ks period monitored by NuSTAR, two periods of duration ∼70 ks were covered by XMM-Newton. In view of the very strong variability of the source, we divide the data into five segments, labeled epochs *a*–*e*, among which epochs *b* and *d* correspond to the periods covered by both satellites. Below we describe the data sets in turn.

2.1. XMM-Newton

I Zw 1 was observed by XMM-Newton twice in 2020. The observations were conducted separately in two revolutions of the satellite on January 12 and 14 in small-window mode (OBSID: 0851990101 and 0851990201; PI: D. R. Wilkins), during each of which the source was observed for ∼70 ks (epochs *b* and *d* in Figure 1).

We extracted the light curve and spectrum from the European Photon Imaging Camera (EPIC) detectors, both pn and metal oxide semiconductor (MOS), with version 19.1.0 of the standard System Analysis Software (SAS). Specifically, we used tasks `epproc` and `emproc` to get the event list, `evselect` to extract the spectrum and light curve, and `arfgen` and `rmfgen` to generate the ancillary response file and redistribution matrix. We checked that no pile-up correction was needed, and that there were no significant background flares. Although the background count rose to ∼0.8 counts s^{-1} during the last 3 ks of the first exposure, the source count also increased to ∼5 counts s^{-1} during the same period; thus, we did not remove this period. We extracted the spectra from a circular region with a 40″ diameter around the source. For the MOS detectors, we extracted background spectra from a 300″ diameter circle in the outer charge-coupled device (CCDs). Similar parameters were used for the pn detector, using a polygon region that avoids chip edges or serendipitous sources. After checking for consistency, we combined the spectra from the MOS1 and MOS2 detectors with the task `epiccombine` to enhance the signal-to-noise ratio (S/N).

We used `rgsproc` to analyze data from the RGS together with data from EPIC, because the resolution of EPIC is insufficient to resolve the narrow atomic lines in the soft band. We followed standard procedures to ensure that all the sources in the field of view of RGS have been identified correctly and that the selected regions centered on the primary source are correctly defined using dispersion-channel and dispersion-cross dispersion images. During both observations, the background count rate was generally well below 0.2 counts s^{-1}, although during the last 3 ks of the first orbit it rose toward 0.4 counts s^{-1}.

As a result of bad pixels in the RGS CCD, important information was lost in the energy range of 0.5−0.61 keV, in which EPIC-PN and MOS1+MOS2 detected a deep absorption trough (mainly resulting from ionized oxygen and nitrogen; see Section 3.2). Moreover, the S/N is very low in the 0.3−0.5 keV range, even after combining RGS1 and RGS2. Consequently, we coadded the RGS1+RGS2 spectra with `rgscombine` and only used the data in the energy range of 0.61−1.5 keV as a supplement to EPIC. Fortunately, most of the key features discussed in this paper lie in the region of 13−20 Å, where both RGS1 and RGS2 have their highest effective area, and by combining them we were able to reach an acceptable S/N in this energy range. We compared the spectra from different detectors of EPIC and RGS, while also checking their background counts and effective area to identify possible contamination from instrumental features. We ignored the band 1.2−1.25 keV of RGS for epoch *b* because of the appearance of a strong feature, together with a sudden drop of effective area by at least a factor of 2 in RGS2. Similar feature is also present in previous study (10 Å; Silva et al. 2018, see their Figure 2). This is likely to be an instrumental artifact.

To help monitor the variability of the source in the optical and ultraviolet bands, we performed aperture photometry of images extracted from the Optical Monitor (OM) using `omichain`, which include 15 exposures observed using the UVW1 filter, three using the UVW2 filter, and two using the *U*, *B*, and *V* filters.

2.2. NuSTAR

The NuSTAR observations were conducted during a 5.3 day exposure between 2020 January 11 and 16 (OBSID 60501030002). We reduced the data using NuSTARDAS v2.1.1. The event lists from each focal plane module (FPM) detector were processed with NUPIPELINE using the latest calibration (version 20210210). Because of the strong variability of the spectral shape, we divided the data into five shorter segments according to the overlap with the XMM-Newton observations (Figure 1). To mitigate against the reduced S/N after the data division, we extracted the spectra and light curve (3−78 keV) using the strategy recommended for faint sources, using a small circular region of 30″ diameter centered on the point source. Following a similar strategy employed by Wilkins et al. (2021), we combined the data from FPMA and FPMB, after checking for internal consistency. Background spectra were extracted from a circular, source-free region of 300″ in diameter. The larger background area more accurately captures the instrumental features.

3. Spectrum Fitting

The 5 day NuSTAR light curve of I Zw 1 shows very strong variability. A number of X-ray flares in the NuSTAR light curve were covered during one of the two XMM-Newton observations, while two strong and narrow X-ray peaks were not fully captured (in epoch *b*; see also Figures 1 and 3). Wilkins et al. (2021, 2022) studied the broadband data in epochs *b* and *d* with detailed relativistic reflection modeling. Focusing on the two XMM-Newton observations, Wilkins et al. (2022) noticed that between the two epochs the photon index suddenly dropped from $\Gamma \approx 2.1$ to 1.9, evidence that the coronal properties change significantly on a timescale of a couple of days. In view of this rapid variability, we use data from all five epochs to perform our spectral analysis, considering the variation of both continuum shape (Section 3.1) and ionized absorbers (Section 3.2). We also compare with previous spectral fitting results in Section 3.3. All the fits are performed using `Xspec` v12.12.0g (Arnaud 1996), minimizing the modified version of the Cash statistic in `Xspec`.

3.1. Continuum Fitting

We first fit the broadband spectrum[7] with a simple cutoff power-law model (`zcutoffpl`) modified by Galactic absorption Wilms et al. 2000. The column density of the `TBabs` model is fixed to $N_{\rm H,Gal} = 4.6 \times 10^{20}$ cm^{-2} (Kalberla et al. 2005). In agreement with previous studies (Silva et al. 2018; Wilkins et al. 2021, 2022), no intrinsic neutral absorption is required statistically. The residuals of the above phenomenological model (Figure 2(b)) leave a moderate excess in the soft band, as is commonly found in narrow-line Seyfert 1 s (e.g., Czerny et al. 2003; Done et al. 2012). Adding a blackbody component (∼0.1 keV for epoch *d*) improves the fit (C-statistic reduced by ΔC-stat = 167), although the broadband spectrum still has wavy residuals in both the soft and harder bands, requiring absorbers at ∼0.5−0.6 keV, a broad Kα line, and a Compton hump at 20−30 keV (Figure 2). The physical nature of the soft excess in AGNs remains controversial (e.g., warm corona or relativistic reflection; García et al. 2019; Xu et al. 2021). In the context of the relativistic reflection model (e.g., Fabian et al. 2002), emission by reflection from optically thick material near the inner disk, smeared by relativistic effects, can also produce an apparent soft excess as well as broad Kα emission.

We implement the self-consistent reflection model RELXILLCP (Dauser et al. 2014; García et al. 2014) to account simultaneously for the soft excess, the broad iron line, and the Compton hump. The thermal Comptonization model for the corona in RELXILLCP is more physical than the cutoff power-law corona spectrum employed in RELXILL, or the power-law

[7] For all the X-ray spectra, we utilize the 0.3−10 keV channels for XMM-Newton EPIC-PN/MOS and the 3−50 keV channels for NuSTAR FPM, within which we have an adequate S/N.

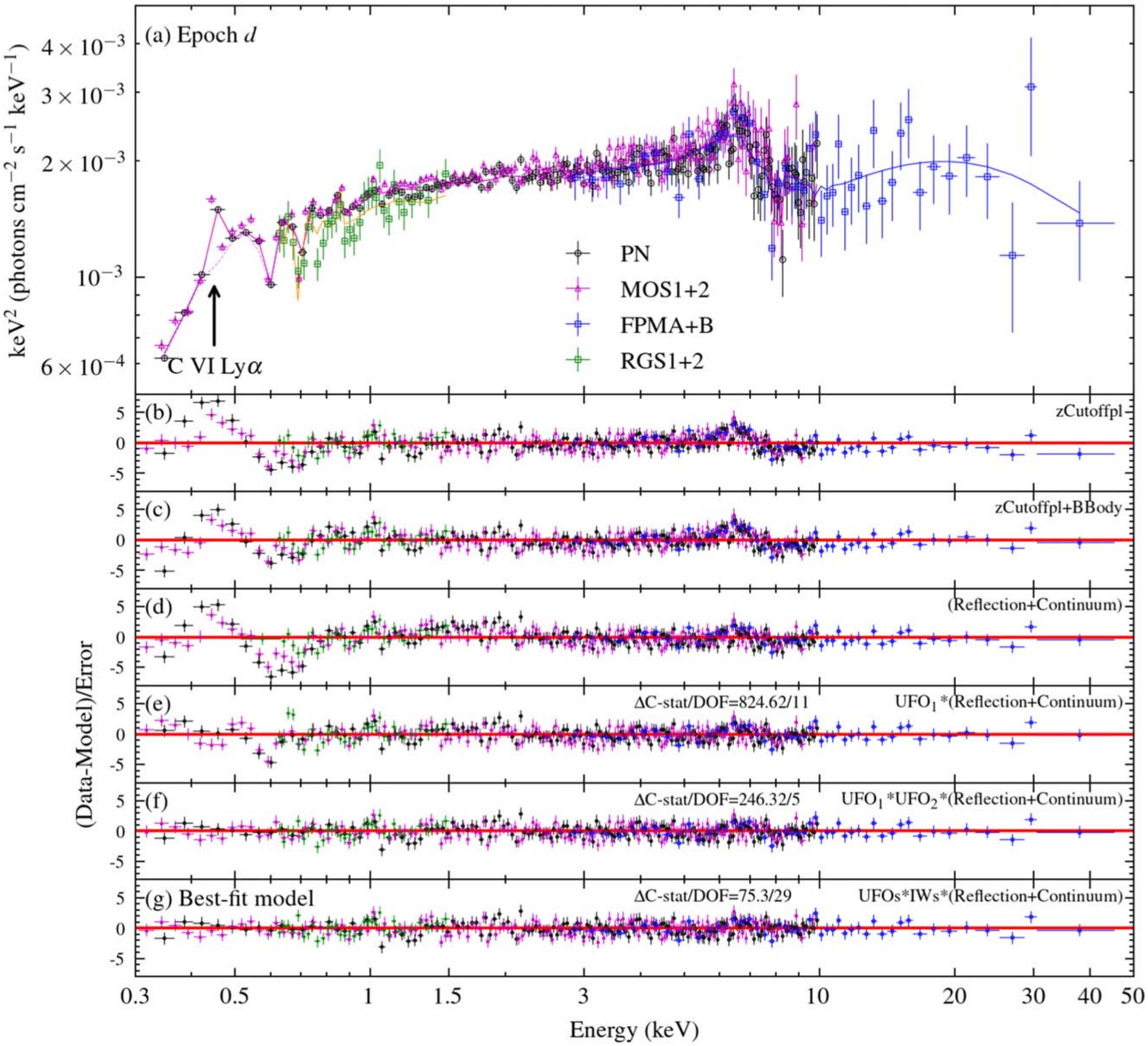

Figure 2. (a) The XMM-Newton and NuSTAR broadband spectra fit with a model that contains three wind components. For clarity, we only show epoch *d* here and the RGS data have been visually rebin to S/N greater than 10. We fit the spectra from different periods simultaneously, tying the spin and inclination angle. Panels (b) and (c) show the improvement of the phenomenological model after adding a blackbody component, indicating that there is a mild soft excess. In panels (d)–(g), we show the improvement of the fit statistic (ΔC-stat; the values are from simultaneously fitting all five epochs) by consecutively adding the UFOs and ionized winds (IWs). Panel (g) is our best-fit model. The mildly broadened emission line at ∼0.45 keV is identified as C VI Lyα (see Section 3.2 for details), which is ubiquitous in low-ionization gas. The requirement of an 8 keV ionized Fe absorber (IW 1) can be clearly seen in panel (f). See Figure 4 for the detailed impact of all IWs and UFOs on the fits.

spectrum with cutoff energy fixed at 300 keV assumed in RELXILLD. All spectra are fitted simultaneously, allowing the normalization to vary between different epochs to account for changes in overall flux, but we tie together the iron abundance, the inclination angle of the accretion disk, and the BH spin. A cross-calibration constant was added for epochs *b* and *d* so as to compensate for their different net exposure times and normalization differences between the EPIC, RGS, and FPM instruments. As the disk size cannot be independently constrained, we freeze the inner disk radius to the value of the innermost stable circular orbit, while fixing the outer disk radius at the default value of 400 r_g, with $r_g = GM/c^2$ the gravitational radius of the BH. The disk emissivity is assumed to be a broken power law with an outer index fixed to 3. The break radius ($R_{\rm break}$) and inner power-law index ($\rm Index_1$) are free to vary.

We generate posterior probability distributions for each parameter using Markov chain Monte Carlo (MCMC) calculations, as implemented in Xspec. Adopting the Goodman–Weare algorithm, we use 200 walkers and a total of 60,000 iterations. We test convergence with the integrated autocorrelation time τ_f (Foreman-Mackey et al. 2013) and a graphical method to monitor the evolution of parameters by plotting their values with regard to MCMC steps. We reject the first 10,000 iteration ($\gtrsim 3\,\tau_f$) steps to ensure that the chain *forgets* where it started. Unless otherwise specified, all error measurements reported in this paper are derived by MCMC calculations and are given at the 90% confidence level for one parameter of interest. The results are shown in Figure 3 and Table 1, after

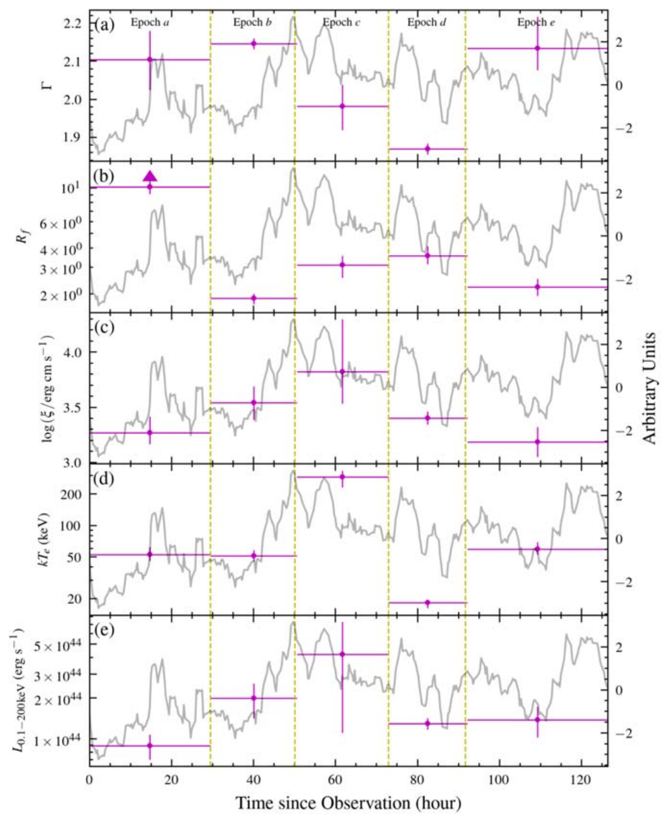

Figure 3. The time evolution of continuum and reflection parameters. The panels show the (a) power-law photon index of RELXILL, (b) reflection fraction, (c) disk ionization parameter, (d) corona temperature, and (e) the 0.1−200 keV luminosity of the power-law component. The smoothed and normalized NuSTAR/FPM count rate is plotted in gray in all the panels. The corona was rapidly heated in epoch *c* to ∼300 keV, after which strong cooling of the corona, together with spectral hardening, was observed in epoch *d*.

incorporating our best-fit ionized absorber model in Section 3.2.

A major X-ray flare occurred toward the end of epoch *b*. The count rate from both XMM-Newton and NuSTAR sequentially increased, as clearly seen in the light curve (Figure 1) and in the smoothed and normalized NuSTAR/FPM count rate (Figure 3), which increased fivefold over a timescale of ∼10 hr in epoch *c*. Meanwhile, an ionized absorption feature around 8 keV emerged after the flare. The next section presents a detailed analysis of this feature.

3.2. Ionized Absorber Fitting

Several ionized absorbers was detected during the five epochs of observations. Including these absorbers in the fit decreased the C-statistic significantly (Column 6 of Table 2). We fit the absorbers with the X-ray atomic code XSTAR (Kallman & Bautista 2001) and applied MPI_XSTAR (Danehkar et al. 2017), assuming $\Gamma = 2$ and solar abundances (Grevesse et al. 1996), considering all elements with $Z < 30$. For the first step, we used the *analytic* model WARMABS to constrain the absorption line width. During the fitting process, WARMABS calls XSTAR *on the fly*, drawing the ion population from a precalculated population file that assumes a power-law input continuum with $\Gamma = 2.2$ and a particle number density of 10^{12} cm^{-3}. We identify five individual ionized absorbers with different turbulence velocities and ionization states. Three of the absorbers match the predictions of an IW (see discussion in Section 4.1), and we designate them IW 1, IW 2, and IW 3, while the other two have velocities substantial enough to be called UFOs; UFO 1 and UFO 2. Since fast outflows ($v_w > 0.1c$) are generally believed to be generated from the innermost regions of the accretion disk (Gofford et al. 2015), after our initial test fitting we modified the iron abundance of the high velocity absorbers to 3 times the solar value to be consistent with the best-fit iron abundance derived by RELXILLCP (see Section 3.1).

The properties of the five ionized absorbers are summarized as follows (Table 2):

1. *UFO 1*: A broad, ultrafast, lower ionization outflow. Broad absorption features near ∼0.62 keV for both epochs *b* and *d* can be seen in the residuals of the reflection model (epoch *d* is shown in Figure 2(d)), which can be attributed to ionized oxygen absorption with turbulence velocity $v_{\rm turb} \simeq 2500$ km s^{-1}. Besides the prominent absorption features, a broad ($v_{\rm turb} \approx 2500$ km s^{-1}) emission feature is detected also at ∼0.47 keV (26 Å) in both the EPIC and RGS spectra. The emission feature is identified as C VI Lyα, and it can be self-consistently fit with an XSTAR reflection line table generated along with the absorber table. Considering the similar turbulence velocity, we link the column density and ionization state of this cold ($\xi \approx 10^{-1}$ erg cm s^{-1}) emitter to that of the cold absorber (UFO 1). Considering both the emission and absorption of UFO 1 improves the fit by ΔC-stat = 824.62 (Figure 2(e)). A similar emission feature has been seen in the narrow-line Seyfert 1 galaxy NGC 4051, which Steenbrugge et al. 2009 interpreted as arising from a stratified broad-line region.
2. *UFO 2*: A broader, ultrafast, moderately ionized outflow. Another broad absorption feature at ∼0.75 keV can be attributed to a higher ionization state of oxygen compared to UFO 1, with a broader turbulence velocity of $v_{\rm turb} \simeq 3600$ km s^{-1}. By considering only the absorption of UFO 2, the fit was improved by ΔC-stat = 246.32 (Figure 2(f)).
3. *IW 1*: A narrow, ultrafast, highly ionized wind. A strong, broad absorption feature at ∼8 keV emerged after the flare (Figures 4(c)–(e)). The absorption can be attributed to Fe XXV/XXVI features from a highly ionized wind with $v \approx (0.1{-}0.2)$ *c* and $v_{\rm turb} \approx 500$ km s^{-1}. If the analysis is confined merely to the average spectrum of epochs *b* and *d*, these features can be accounted with Gaussian absorption models, although the improvement of the fit is insignificant ΔC-stat ≈6; Wilkins et al. 2021). However, incorporating epochs *c* and *e* and fitting all epochs simultaneously improves the fit by ΔC-stat = 20.73.
4. *IW 2 and IW 3*: Two narrow, moderately fast, highly ionized winds. To minimize the narrow emission features in RGS residuals (Figure 4(f), (g)), we add to our model two extra photoionized components, calculated by XSTAR assuming solar abundance, an input power-law spectrum with $\Gamma = 2.0$, and a turbulence velocity $v_{\rm turb} \approx 500$ km s^{-1}. We consider both reflected and transmitted emission, such that for these two absorbers we include a total of four additive tables. We fix the column density and ionization state of all emitters to those of the corresponding absorbers. These tables well describe the narrow substructure in the RGS spectra at

Table 1
Best-fit Parameters for the Continuum

Epoch (1)	a_* (2)	i (°) (3)	$A_{\rm Fe}$ (4)	kT_e (keV) (5)	Γ (6)	R_f (7)	Index$_1$ (8)	$R_{\rm break}$ (r_g) (9)	$\log\xi$ (erg cm s^{-1}) (10)	$L_{0.1-200\ \rm keV}$ (10^{44} erg s^{-1}) (11)
a				$52.2^{+9.3}_{-6.4}$	2.10 ± 0.08	>9.08	$8.7^{+1.2}_{-1.5}$	$2.66^{+0.30}_{-0.34}$	$3.27^{+0.15}_{-0.10}$	0.89 ± 0.18
b				$50.9^{+7.1}_{-5.7}$	2.15 ± 0.01	$1.86^{+0.13}_{-0.16}$	$9.6^{+0.4}_{-1.4}$	$2.36^{+0.17}_{-0.21}$	3.54 ± 0.15	1.98 ± 0.56
c	>0.973	$42.3^{+2.4}_{-2.2}$	$3.51^{+0.37}_{-0.52}$	289^{+43}_{-60}	1.98 ± 0.06	$3.09^{+0.47}_{-0.55}$	>10	$2.23^{+0.14}_{-0.21}$	$3.82^{+0.47}_{-0.29}$	4.20 ± 3.10
d				$18.2^{+1.2}_{-2.0}$	1.87 ± 0.01	$3.55^{+0.57}_{-0.43}$	>10	$2.49^{+0.10}_{-0.09}$	3.40 ± 0.06	1.29 ± 0.12
e				$59.1^{+9.6}_{-6.7}$	2.14 ± 0.05	$2.21^{+0.29}_{-0.28}$	$9.3^{+0.7}_{-2.7}$	$1.84^{+0.14}_{-0.16}$	$3.18^{+0.14}_{-0.13}$	1.38 ± 0.35

Note. Column (1): epoch. Column (2): dimensionless BH spin. Column (3): inclination angle of the accretion disk. Column (4): iron abundance. Column (5): corona temperature. Column (6): photon index of the RELXILL model. Column (7): reflection fraction. Column (8): power-law index 1 for the broken power-law disk emissivity. Column (9): break radius for the broken power-law disk emissivity, in units of the gravitational radius $r_g = GM/c^2$. Column (10): accretion disk ionization parameter. The spin, inclination, and iron abundance are fitted simultaneously for the five epochs. Column (11): 0.1–200 keV luminosity of the power-law component.

~14 and 18 Å. The fit is improved by ΔC-stat ≈54. Since the redshift of the emission lines is consistent with that of the absorbers within statistical error, we link them in the following analysis. The RGS and EPIC data generally agree well in 0.61–1.5 keV. We label the most prominent emission features with the corresponding absorbers in Figure 4.

To assess the significance of the IW 1 features and the possibility of instrumental artifacts,[8] we run a series of Monte Carlo simulations according to the procedure described in Tombesi et al. (2010), using the `fakeit` command built-in `Xspec` to quantify the incidence of spurious lines when blindly searching for features between 7 and 9 keV. We adopt the best-fit model shown in Figure 2(f) (with IW 1 removed from the model). Our goal is to test the null hypothesis that the model without IW 1 already can describe the data satisfactorily. We simulate 1000 sets of observations with both the XMM-Newton and NuSTAR detectors using the same exposure time as the actual observations. To check the probability of detecting a Gaussian absorption trough due to random fluctuations of the simulated data, we add a Gaussian absorption component to the baseline model with its line centroid randomly assigned between 7 and 9 keV while fixing its line width to the best-fit, observed value. The normalization is left free to vary. Setting ΔC-stat = 18 as the significance threshold, as observed in the real data, we find that ~15% of the simulated spectra produce spurious lines that improve the fit by an amount greater than the significance threshold. We conclude that the significance for a single Gaussian absorption feature in our data is 85%. The absorption feature actually observed in our data is a double Gaussian, corresponding to highly ionized species of Fe XXV and Fe XXVI broadened by $v_{\rm turb} \approx 500$ km s^{-1} (Figures 4(c)–(e)). Including this component, our final model,[9] which contains five XSTAR absorbers and five XSTAR additive tables, produces a good fit with C-statistic/DOF = 1306.77/1250.

3.3. Comparison with Previous Work

There have been six previous studies of the X-ray properties of I Zw 1 using XMM-Newton observations. Gallo et al. (2004) analyzed an ~20 ks observation taken in 2002, detecting a broad iron line, a hard X-ray flare, and spectral hardening during the flare, a result consistent with the notion that magnetic reconnection heats the corona of the accretion disk (Merloni & Fabian 2001). Silva et al. (2018) conducted two observations through XMM-Newton in 2015 (total exposure of ~270 ks), detecting absorption in the soft X-rays by two components of WAs with a similar column density and ionization parameter. The 2015 observations were also analyzed by Reeves & Braito (2019), who proposed that the broad iron K profile can be well fit with a wide-angle accretion disk wind. Wilkins et al. (2021, 2022), with the same data set used here, investigated the timing and spectral variability of I Zw 1. Examining the 3−50 keV spectrum secured by combining observations from XMM-Newton and NuSTAR, these authors argued that the broadened iron K fluorescence line centered at 6.4 keV, its redshifted wing extending to 3 keV, and the Compton hump around 25 keV can be well described by a model comprised of continuum emission from the corona and its reflection from an accretion disk around a rapidly spinning ($a_* > 0.94$) BH.

Broad Fe Kα emission was present in all the observations above. Reeves & Braito (2019) tried three different continuum models to account for the broad Fe Kα emission, which they argued comes from a persistent, wide-angle wind. They also showed that the spectra can be fit with three different models, namely XSTAR, a P Cygni profile (Done et al. 2007), and the disk wind model developed by Sim et al. (2008), which enabled them to derive the mechanical power and momentum rate of the fast wind. The mass and momentum rates inferred from these three models are comparable, although rather arbitrary assumptions were made regarding the outflow location and launching radius. Specifically, they set the wind location to the escape radius of the BH, which in practice places a lower limit on the mass outflow and momentum rates. The same assumption was made for their disk wind simulation. They found a momentum rate consistent with the AGN photon momentum, a condition corresponding to a near-Eddington outflow (King 2003; King & Pounds 2015), from which they concluded that a powerful, large-scale, energy-conserving wind can be ruled out in I Zw 1 (see Section 4.3 for a discussion of the implications).

Wilkins et al. (2021) included relativistic reflection models in their continuum analysis. They implemented a twice-broken power-law emissivity profile for the accretion disk, but both the middle and outer power-law indices were not well constrained. Using a similar reflection model (KDBLUR3*XILLVER), Wilkins

[8] The XMM-Newton EPIC-PN detector contains known instrumental lines in the region of 7−9 keV, such as Cu Kα at 8.048 keV (see Jansen et al. 2001).
[9] In the terminology of `Xspec`, the best-fit model is constant*TBabs*(XSTAR*RelxillCp+XSTAR$_{\rm emission}$).

Table 2
Best-fit Parameters for the Ionized Absorbers

Component	Epoch	$N_{\rm H}$ (10^{20} cm^{-2})	$\log \xi$ (erg cm s^{-1})	v_w/c	ΔC-stat/DOF
(1)	(2)	(3)	(4)	(5)	(6)
UFO 1	*b*	$2.09^{+0.25}_{-0.31}$	$-1.72^{+0.14}_{-0.12}$	0.34 ± 0.01	824.62/11
	d	2.45 ± 0.21	$-0.711^{+0.035}_{-0.037}$	$0.276^{+0.008}_{-0.010}$	
UFO 2	*b*	$7.07^{+0.87}_{-0.82}$	$0.85^{+0.12}_{-0.08}$	$0.112^{+0.0008}_{-0.0013}$	246.32/5
	d	$3.44^{+0.32}_{-0.37}$	$0.283^{+0.026}_{-0.025}$	$0.124^{+0.009}_{-0.006}$	
IW 1	*c*	4790^{+590}_{-410}	$3.44^{+0.16}_{-0.36}$	$0.25^{+0.02}_{-0.03}$	20.73/9
	d	495^{+47}_{-39}	$3.64^{+0.14}_{-0.32}$	$0.22^{+0.02}_{-0.03}$	
	e	2270 ± 180	$3.94^{+0.36}_{-0.46}$	$0.27^{+0.02}_{-0.04}$	
IW 2	*b*	2.46 ± 0.29	$1.82^{+0.21}_{-0.27}$	$0.035^{+0.004}_{-0.004}$	17.93/10
	d	$1.38^{+0.11}_{-0.07}$	$1.034^{+0.047}_{-0.051}$	$0.036^{+0.003}_{-0.002}$	
IW 3	*b*	$6.16^{+0.37}_{-0.33}$	0.695 ± 0.063	0.044 ± 0.001	36.64/10
	d	$2.42^{+0.32}_{-0.21}$	$1.21^{+0.11}_{-0.08}$	0.046 ± 0.001	

Note. Column (1): component. Column (2): epoch. Column (3): hydrogen column density. Column (4): ionization parameter. Column (5): outflow velocity divided by the speed of light. Column (6): improvement of the C-statistic and the corresponding variation of the degree of freedom (DOF) after adding this component.

et al. (2022) argued that a twice-broken power law is preferred over a single power law, although the validation is restricted in 3−10 keV, focusing only on the broad iron Kα line (see their Figure 6). However, since Wilkins et al. (2021, 2022) used KDBLUR3 to convolve XILLVER, the convolution of the reflected spectra was not radius dependent, which is required so as to calculate the correct contribution of the multiple angular solutions to a given viewing angle (García et al. 2014). This problem undermines their argument that the twice-broken power law is superior. Our analysis indicates that the broken power-law emissivity self-consistently implemented by RELXILLCP can fit the broadband shape satisfactorily. While Wilkins et al. (2022) argued that it is necessary to account for the gradient in the ionization of the disk to describe the broadband (0.3−50 keV) spectrum, in Section 3.2 we show that the mismatch between the soft excess and broad iron Kα may be due to the absorption at ∼0.6 and 0.7 keV. There is no need to consider an ionization gradient after adding appropriate absorbers (see Figure 2 and corresponding discussion in Section 3.2). Our measured value of the spin, $a_* > 0.973$, consistent with that found by Wilkins et al. (2022), supports a maximally spinning supermassive BH. However, our derived values of iron abundance ($A_{\rm Fe} \approx 3.5$) and disk inclination angle ($i \approx 42.3°$) are slightly smaller than previously reported.

The average X-ray luminosity of the corona, following a trend similar to the disk ionization parameter ξ, increased from $\sim 1 \times 10^{44}$ erg s^{-1} to a peak value of 5×10^{44} erg s^{-1} during epoch *b*, while keeping an almost constant corona temperature. After the main flare in epoch *c*, the X-ray luminosity quickly dropped to $\sim 1.5 \times 10^{44}$ erg s^{-1}, which was maintained through the last two epochs. The corona electron temperature changed anomalously after the flare: after rapidly surging during epochs *b* and *c*, the temperature decreased to ∼18 keV in epoch *d*. The reflection fraction R_f in epoch *a* was a lower limit (note that the soft upper limit for it is 10) and declined rapidly to ∼1. It kept rising through epochs *b*–*d* until reaching ∼3 in epoch *d*, and then during the last epoch it returned to the same level as epoch *b*. The evolutionary trend for the photon index is just the reverse of that for R_f, fluctuating between $\Gamma \approx 1.9$ and 2.1. There is no obvious correlation between Γ and X-ray luminosity, although adding a 20 hr time lag to Γ would produce an inverse correlation. Most of the continuum parameters (Γ, $E_{\rm cut}$ or kT_e, R_f) derived in this work follow qualitatively the same trends found by Wilkins et al. (2022), although our R_f is generally larger by an order of magnitude. This may be due to the different implementation of relativistic blurring by KDBLUR3*XILLVER and RELXILLCP.

Costantini et al. (2007) and Silva et al. (2018) detected in the soft X-ray band of RGS two low-velocity ($v_w \approx 1000$ km s^{-1}) WA components, which have $N_{\rm H} \approx 10^{20}$–$10^{21}$ cm^{-2} and $\xi \approx 1$−100 erg cm s^{-1}. The rms width of the absorption lines was constrained in their fit to be ∼70 km s^{-1}, significantly smaller than RGS energy resolution of ∼700 km s^{-1} (XMM-Newton Users Handbook, Table 8). Our fits do not require WA ($v_w < 0.01c$) components. Adding an extra XSTAR table (assuming $v_{\rm turb} = 500$ km s^{-1} as before, or 70 km s^{-1} as derived by Silva et al. 2018) or `warmabs` components has only a negligible impact on the fit (ΔC-stat < 1). It is worth mentioning that all previously reported lines are extremely narrow, having $v_{\rm turb} \approx 30 - 100$ km s^{-1}, well below the resolving capability of EPIC. In addition, the most prominent oxygen edges are at 23−25 Å (Silva et al. 2018), where our RGS data, unfortunately, lose most information due to bad pixel and have poor S/N (see also Section 2, Figure 4(f), (g)). We do note, however, that WAs may actually be the by-product of fast outflows. Repeated shocks produced by an outflow can leave behind heated and compressed gas, which may linger for some time before dispersing or falling back to the BH. Such material may form much of the WAs frequently observed in AGNs (King 2010a; Pounds & King 2013). Moreover, for an interstellar medium of sufficiently low density, the shock will be weak, and the launched WA will have small covering factor (Bu & Yang 2021), conditions that may easily lead to a low detection fraction during a single observational campaign. This may explain the non-detection of previously reported WAs in our data. These issues will be discussed further in Section 4.1, where we argue that WAs may be the post-shock material associated with the fast, ionized wind.

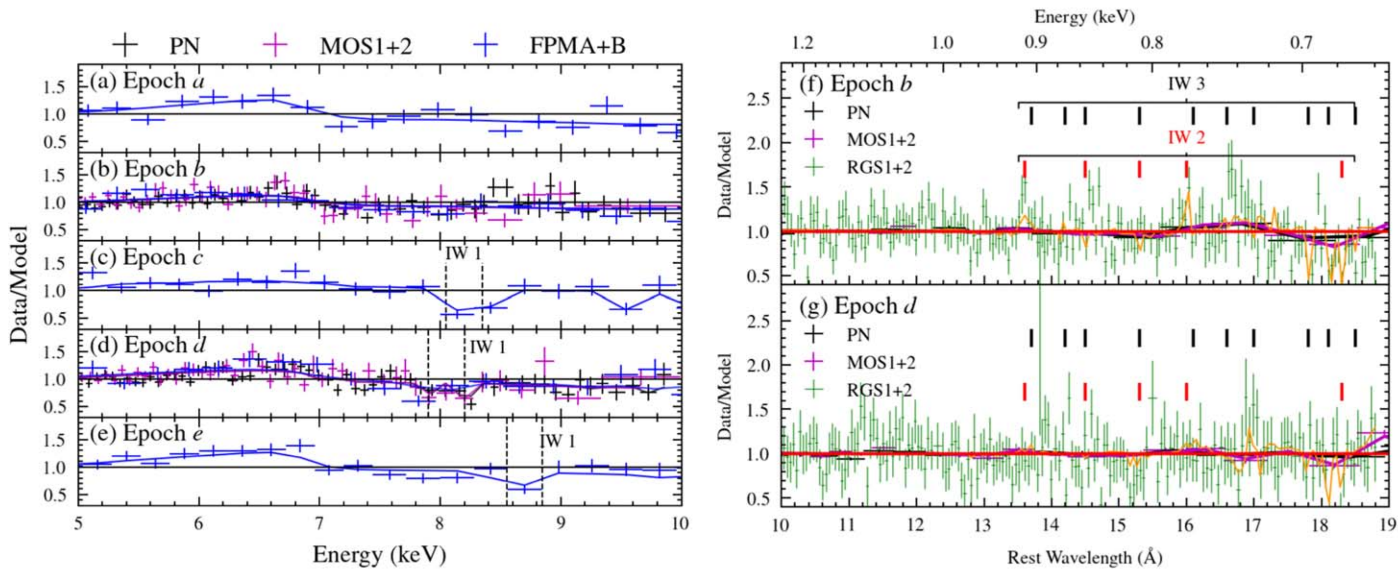

Figure 4. Panels (a)–(e): the ratio between data points and the fit of a phenomenological model consisting of a redshifted cutoff power law and a blackbody, for observations during epochs *a*–*e*. Panels (f) and (g): the ratio between data points and the best-fit model with UFOs included, as already shown in Figure 2(f). Our best-fit model (five XSTAR components) is superimposed with the same color as the data points, but for observations during (f) epoch *b* and (g) epoch *d*, our best-fit model (five XSTAR components) for RGS1 + 2 is superimposed in orange. The broad Fe Kα line at 6.4 keV can be clearly seen. We note the emergence during (c) epoch *c* of a variable Fe absorber (ionized wind 1; IW 1) at $\sim$8−9 keV, whose profile can be described by a double Gaussian. In (f) and (g), the components associated with IW 2 and IW 3 are marked.

4. Discussion

4.1. Physical Properties of the Absorbers

To understand the origin of the outflowing absorbers and their connection with the feedback process, it is important to estimate their physical distance from the central BH as well as other physical properties such as their outflow energy and momentum rate. Compared with energy-driven (hot, thermal interaction) outflows, momentum-driven (cool, ram-pressure interaction) outflows have only a negligible effect on the galaxy bulge (see also Section 4.3).[10] Energy-driven shocks may very well operate in I Zw 1, in light of the high energy-transfer rate ($\dot{E}_{k,\mathrm{molecular}}/\dot{E}_{k,\mathrm{UFO}}$) deduced by Mizumoto et al. (2019). The kinetic energy of the UFO might be underestimated because Mizumoto et al. (2019) provide only a lower limit for the kinetic energy. The same concern applies to the analysis of Reeves & Braito (2019), as mentioned in Section 3. Taking this caveat into consideration for I Zw 1 would weaken the correlation between λ_{Edd} and energy-transfer rate presented in (Mizumoto et al. 2019, their Figures 6 and 7). We apply the following equations, based on Blustin et al. (2005) and Gofford et al. (2015), to give a more physical description of the ionized absorbers:

$$\dot{M}_w = \mu \Omega b R^2 m_p n(R) v_w, \tag{1}$$

$$\dot{K}_w = \frac{1}{2}\dot{M}_w v_w^2, \tag{2}$$

$$\dot{P}_w = \dot{M}_w v_w, \tag{3}$$

$$\delta R \simeq N_{\mathrm{H}}/bn, \tag{4}$$

where $\dot{M}_w$ is the mass outflow rate, $\dot{K}_w$ is the kinetic energy rate, $\dot{P}_w$ is the momentum rate, and δR is thickness of the outflow layer. We set the mean particle mass number $\mu \simeq 1.23$ based on cosmic elemental abundances (75% hydrogen and 25% helium), with R the distance between the wind and the central radiation source, n the particle number density, m_p the proton mass, and v_w the outflow velocity. The solid angle of the outflow is taken to be $\Omega = 0.4 \times 4\pi$. The clumpiness of the wind is described by the parameter b, with $b = 1$ corresponding to a smooth outflow. Historically, the escape radius of the outflow is often used to provide a lower limit for the location of the observed outflow,

$$R_{\min} = \frac{2GM_\bullet}{v_w^2}.$$

An upper limit for the outflow location follows from the assumption that the cloud fully fills the space between the observed outflow layer and the source, namely, $N_{\mathrm{H}} = nR_{\max}$, such that

$$R_{\max} = \frac{L_{\mathrm{ion}}}{\xi N_{\mathrm{H}}},$$

where $\xi \equiv L_{\mathrm{ion}}/nR^2$ is the ionization parameter, and we fix the ionizing luminosity[11] $L_{\mathrm{ion}} \simeq 1.5 \times 10^{45}$ erg s^{-1}. However, the conventionally estimated values of $R_{\max}$ are generally very loose. We obtain $R_{\max} \approx 1$ Mpc for UFO 1 and UFO 2, and $\sim$100 kpc for IW 2 and IW 3. Only IW 1 has a more meaningful value of $R_{\max} = 0.36^{+0.17}_{-0.15}$ pc. The estimated values of $R_{\min}$ for UFO 1, UFO 2, and IW 1 are very close to the BH ($\sim 100 r_g$), while for IW 2 and IW 3 $R_{\min} \approx 1000 r_g$.

The best-fit results summarized in Table 2 indicate that the ionization state of the absorbers is highly variable, but, with the exception of IW 1, seemingly is uncorrelated with the X-ray luminosity. For instance, the X-ray luminosity of I Zw 1 during

[10] These are also referred to as energy-conserving and momentum-conserving outflows, respectively.

[11] We estimate $L_{\mathrm{ion}} \simeq L_{\mathrm{bol}}/2$, assuming for I Zw 1 a model spectrum energy distribution described by a series of power laws having three break points (Reeves & Braito 2019).

Table 3
Physical Properties of the UFOs

Component	$v_{\rm turb}$ (km s^{-1})	$R_{\rm MAD}$	b	δR	$\dot{K}$ ($L_{\rm bol}$)	$\dot{P}$ ($L_{\rm bol}/c$)
(1)	(2)	(3)	(4)	(5)	(6)	(7)
UFO 1	2500	$1.8^{+3.1}_{-0.6} \times 10^{-2}$ pc	$2.92^{+0.50}_{-4.86} \times 10^{-8}$	358^{+2313}_{-328} $R_{\rm S}$	1 (frozen)	$6.53^{+0.18}_{-0.13}$
UFO 2	3600	$1.05^{+0.48}_{-0.73} \times 10^{-2}$ pc	$3.3^{+0.66}_{-0.62} \times 10^{-5}$	16^{+15}_{-14} $R_{\rm S}$	1 (frozen)	$16.92^{+0.72}_{-0.66}$
IW 1	500	4999^{+1388}_{-2059} $R_{\rm S}$	1 (frozen)	62^{+30}_{-29} $R_{\rm S}$	204^{+121}_{-112}	1643^{+909}_{-846}
IW 2	500	$4.3^{+4.0}_{-2.9} \times 10^{-2}$ pc	$9.1^{+5.4}_{-3.9} \times 10^{-3}$	$2.8^{+6.0}_{-2.5}$ $R_{\rm S}$	1 (frozen)	$56.6^{+4.5}_{-5.3}$
IW 3	500	$1.65^{+0.48}_{-1.02} \times 10^{-2}$ pc	$1.34^{+0.19}_{-0.16} \times 10^{-3}$	$1.8^{+1.3}_{-1.6}$ $R_{\rm S}$	1 (frozen)	$44.18^{+0.96}_{-0.68}$

Note. Column (1): component. Column (2): turbulent velocity. Column (3): distance from the radiation source to the wind, using the MAD method; $R_{\rm S} = 2GM/c^2$ is the Schwarzschild radius. Column (4): volume-filling factor, which describes the clumpiness of the outflow; smaller b means that the gas is filling less space, and thus has higher clumpiness. Column (5): thickness of the wind layer. Column (6): outflow kinetic luminosity. Column (7): outflow momentum luminosity.

epochs b and d was quite similar, but the ionization state of the absorbers varied wildly. The rapid variability can be explained with a picture in which the shell wind along the line of sight is clumpy, as a consequence of, for instance, Plateau–Rayleigh instability. The shell's apparent thickness then depends on the particular clump that we are observing, not on the intrinsic variability of the velocity or the physical properties of the gas in the clump. To better constrain the physical properties of the winds, we use the median absolute deviation (MAD) of $N_{\rm H}$ and v_w to estimate the density of the outflows (Serafinelli et al. 2019). This method assumes that the shell's apparent thickness is $\delta R = N_{\rm H}/bn$ (Equation (4); a factor of order unity was dropped for simplicity), that the average density of the shell does not vary significantly (i.e., $\Delta n/\Delta t \simeq 0$), and that the median deviation of the velocity is $\Delta v_w = \Delta(\delta R)/\Delta t$. Taking the time derivative of both sides of Equation (4),

$$\frac{\Delta N_{\rm H}}{\Delta t} = bn\frac{\Delta(\delta R)}{\Delta t} + b\delta R\frac{\Delta n}{\Delta t},$$

and the typical shell density can be expressed as

$$\langle n\rangle = \frac{\Delta N_{\rm H}}{b\Delta t\Delta v_w}.$$

It then follows that the distance of the absorbers from the BH is

$$R_{\rm MAD} = \sqrt{\frac{L_{\rm ion}}{\langle n\rangle\xi}}. \tag{5}$$

The physical quantities estimated by Equations (1)–(5) are listed in Table 3. The relative error of $R_{\rm MAD}$ is high due to the differential operation, which significantly amplifies the relative error in $N_{\rm H}$ and v_w. Assuming that during epoch c ($\Delta t = 69.3$ ks) the average density of the shell does not vary significantly, we can obtain $R_{\rm MAD}$, and hence a number of physical properties, for the outflows detected during our observations. It should be noted that the mass outflow rate and the corresponding momentum and energy rates do not depend on the specific method used to estimate the distance (except for $R_{\rm min}$, where the photoionization equilibrium is not considered). Combining Equation (1) with the definition of the ionization parameter, we can obtain

$$\dot{M} = \frac{\mu m_p L_{\rm ion} b v\Omega}{\xi},$$

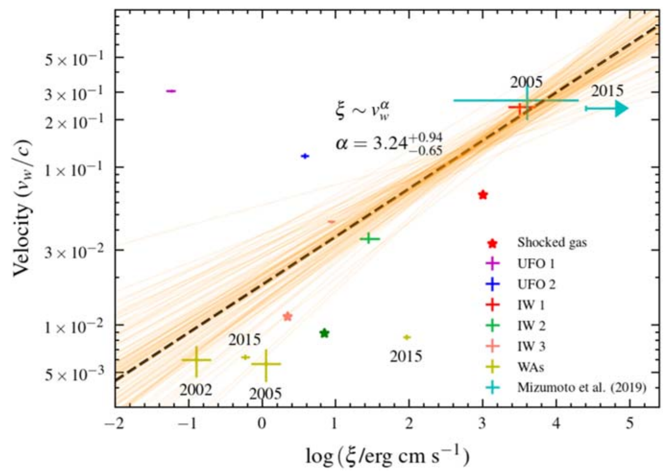

Figure 5. Correlation between the outflow velocity and the ionization parameter of all outflows detected since 2002. We plot all WAs and ionized absorbers reported by Silva et al. (2018) and Mizumoto et al. (2019) in 2002, 2005, and 2015 observations, except those with no constraints on velocity. A linear fit in log-log space for the highly ionized winds detected in epoch b, epoch d, and 2005 yields $\xi \sim v_w^{3.24^{+0.94}_{-0.65}}$, which agrees well with the analytic result given in Equation (8). To show the error distribution, we plot 100 samples from the chain in orange. This means that IW 2 and IW 3 may have the same origin as IW 1, and that the previously detected WAs are all likely to be gas shocked by the highly ionized, super-Eddington IWs. The predicted positions of shocked outflows are marked with asterisks, whose colors indicate the corresponding pre-shock outflows.

which is proportional to the outflow's clumpiness b. The exact value of b is hard to be observed directly, even though it has been argued that in highly ionized outflows, such as IW 1 in I Zw 1, we can assume $b = 1$ (Gofford et al. 2015).

We estimate the clumpiness parameter b by taking advantage of the general physical properties of a super-Eddington outflow. Given the BH mass of $M_\bullet = 9.3 \times 10^6\, M_\odot$ determined through reverberation mapping (Huang et al. 2019) and the bolometric luminosity of $L_{\rm bol} = 3 \times 10^{45}$ erg s^{-1} (Porquet et al. 2004; Martínez-Paredes et al. 2017), I Zw 1 formally qualifies as a super-Eddington source with $\lambda_{\rm Edd} = 2.58$. Additional arguments are given in Figure 5 and Section 4.2 that the IWs in I Zw 1 are likely associated with a super-Eddington wind. Under these conditions, matter is blown away in almost all directions outside the equatorial plane, with mechanical luminosity comparable to the photon luminosity according to simulations (Hashizume et al. 2015; Jiang et al. 2019). Setting

$\dot{K} = L_{\rm bol}$ (King & Muldrew 2016),

$$b = \frac{2\xi L_{\rm bol}}{\mu m_p L_{\rm ion} v^3 \Omega}. \quad (6)$$

Apart from IW 1, for which we assume $b = 1$, we use Equation (6) to derive b and the distance and momentum rates (Table 3). Note that if we set $b = 1 \times 10^{-2}$ for IW 1, the corresponding kinetic rate will be $\dot{K} \approx L_{\rm bol}$, consistent with the super-Eddington wind assumption.

Compared with the properties of its molecular outflow (Cicone et al. 2014; Shangguan et al. 2020), our results show that IW 1 in I Zw 1 may be momentum driven because both its energy rate and momentum rate are significantly larger than the upper limit for the molecular outflow. This means that IW 1 has been cooled sufficiently and dispersed before interacting with the galaxy bulge. We warn readers that the quantities listed in Table 3 are only order-of-magnitude estimates. The uncertainties consider only the statistic errors of best-fit parameters and are likely unrealistic.

Our result differs from that of Reeves & Braito (2019), who found that the momentum rate of the outflow is comparable with the photon momentum. We note that their analysis focuses on the broad Fe Kα profile, assuming a continuous, persistent disk wind and a simple power-law continuum without any disk reflection feature. In addition, they used the escape distance to estimate the properties of the outflow, as a consequence of which the mass outflow rate, mechanical luminosity, and momentum rate may have been underestimated. The duration of one observation epoch in our data ($\sim$70 ks) is already large enough for a wind with $v_w \approx 0.2c$ traverse a few hundred r_g, while the typical escape distance for the outflow is well within a hundred r_g. More importantly, as argued by King & Pounds (2015), we typically observed these outflows a few weeks or months later after the launching event.

4.2. Outflow Efficiency

The efficiency of energy transfer from the disk radiation to the outflow ($\zeta \equiv \dot{K}_w / L_{\rm bol}$) depends largely on the optical depth (τ) of the outflow at the outflow launching location (King & Muldrew 2016). A radiation pressure-driven wind is believed to originate from the inner disk, where locally $L \gtrsim L_{\rm Edd}$ to acquire enough radiation pressure (Shakura & Sunyaev 1973). Meanwhile, τ predominantly depends on the properties of the inner accretion flow (King 2003; King & Muldrew 2016): $\tau \approx 1$ for $\dot{m}_{\rm Edd} \equiv \dot{M}_\bullet / \dot{M}_{\rm Edd} \sim 1$, and $\tau \gg 1$ for $\dot{m} \gg 1$ disk, as further evidenced by numerical simulations (Ohsuga & Mineshige 2011; Hashizume et al. 2015). For a super-Eddington source, the strong coupling between the outflow and the AGN radiation field ($\tau \gg 1$) imposes the energy condition at the launching radius (King & Muldrew 2016),

$$\dot{K}_w = \frac{1}{2}\dot{M}_w v_w^2 \simeq \zeta L_{\rm bol}. \quad (7)$$

The outflow efficiency ζ here is of order unity, typically smaller than 1, since not all the accretion luminosity is available to drive the wind because of the beaming effect in the direction of the BH spin for a super-Eddington disk (King & Muldrew 2016; Jiang et al. 2019).[12] Since there is almost no variability in the 15 XMM-Newton/OM UVM2 exposures for I Zw 1, we assume that the continuum spectrum does not change its shape significantly, retaining the ionization luminosity with $L_{\rm bol}$ as $L_{\rm bol}/L_{\rm ion} \simeq 2$. Combining this with Equation (7) and slightly modifying Equation (6), we obtain the relation between ξ and outflow velocity v_w:

$$\xi \simeq \frac{1}{4\zeta}\Omega b \mu m_p v_w^3 \propto v_w^3. \quad (8)$$

Equation (8) implies that $\xi \propto v_w^3$ for a super-Eddington wind. This relation is modified for near-Eddington ($\dot{m} \approx 1$) AGNs because of the lower optical depth at the outflow launching radius. Under a single-scatter approximation ($\tau \approx 1$; Blustin et al. 2005; King 2010a),

$$\dot{P}_w \equiv \dot{M}_w v_w \simeq L_{\rm bol}/c,$$

which, for an $\dot{m} \approx 1$ accretion flow, establishes a relation between outflow velocity v_w and the outflow energy efficiency

$$\zeta' \equiv \frac{\dot{M}_w v_w^2}{2L_{\rm bol}} = \frac{v_w}{2c}. \quad (9)$$

Following the same procedure used to derive Equation (8), we therefore expect $\xi \propto v_w^2$ for a near-Eddington accretion wind (see also King & Pounds 2015).

Figure 5 summarizes all absorbers detected in I Zw 1, including the WAs reported by Silva et al. (2018) and the UFOs discussed in Mizumoto et al. (2019). The velocities and ξ shown in Figure 5 are all average values, weighted by the exposure time. The IWs follow an apparent linear trend. We perform a linear fit in $\log\xi - \log v_w$ space for the absorbers detected in epoch b, epoch d, and 2005, during which time the IWs had similar properties, considering only the uncertainties in the velocity measurement and assuming that the quoted uncertainties are Gaussian and underestimated by a constant fractional amount. The fit uses the parameters in Table 2 instead of the average values in Figure 5. Employing an MCMC method to derive the posterior probability distribution and uncertainties, the chain for this simple model quickly converges within 100 steps (with $\tau_f \simeq 50$) and 100 burn-in step; the orange curves in Figure 5 are 100 random samples drawn from the chain. The best-fit relation,

$$\log\xi = (3.24^{+0.94}_{-0.65})\log v_w - 28.2^{+6.1}_{-9.3},$$

is consistent with the expectations of a super-Eddington wind, for which $\xi \propto v_w^3$. In principle, launching a locally optically thick outflow typically requires $\dot{m}_w \equiv \dot{M}_w/\dot{M}_{\rm Edd} \sim \dot{m}_{\rm Edd} > 10$ (Middleton et al. 2014). With a luminosity Eddington ratio $\lambda_{\rm Edd} \simeq 2.58$, I Zw 1 could reasonably have an accretion Eddington ratio $\dot{m}_{\rm Edd} \gtrsim 50$ (Ohsuga & Mineshige 2014), since photon trapping significantly suppresses the radiation efficiency in a super-Eddington flow (Abramowicz et al. 1988), and beaming in the direction of the BH spin can further lower the apparent luminosity (Jiang et al. 2019). Note that WAs with no constraints on velocity are not considered in our analysis (e.g., WA 2 in Costantini et al. 2007).

To investigate the consequences of their interaction with the interstellar medium, we overlay in asterisks in Figure 5 the positions of shocked outflows predicted by the classical Rankine–Hugoniot relations, assuming conditions for a normal isothermal shock (for an early application of this method, see King 2010a and Pounds & King 2013). The location of the post-shock gas for IW 1 is marked in red. Given the position of IW 1, it is clear that IW 2 and IW 3 are unlikely to be associated

[12] The ζ adopted here is equivalent to l'/l in King & Muldrew (2016).

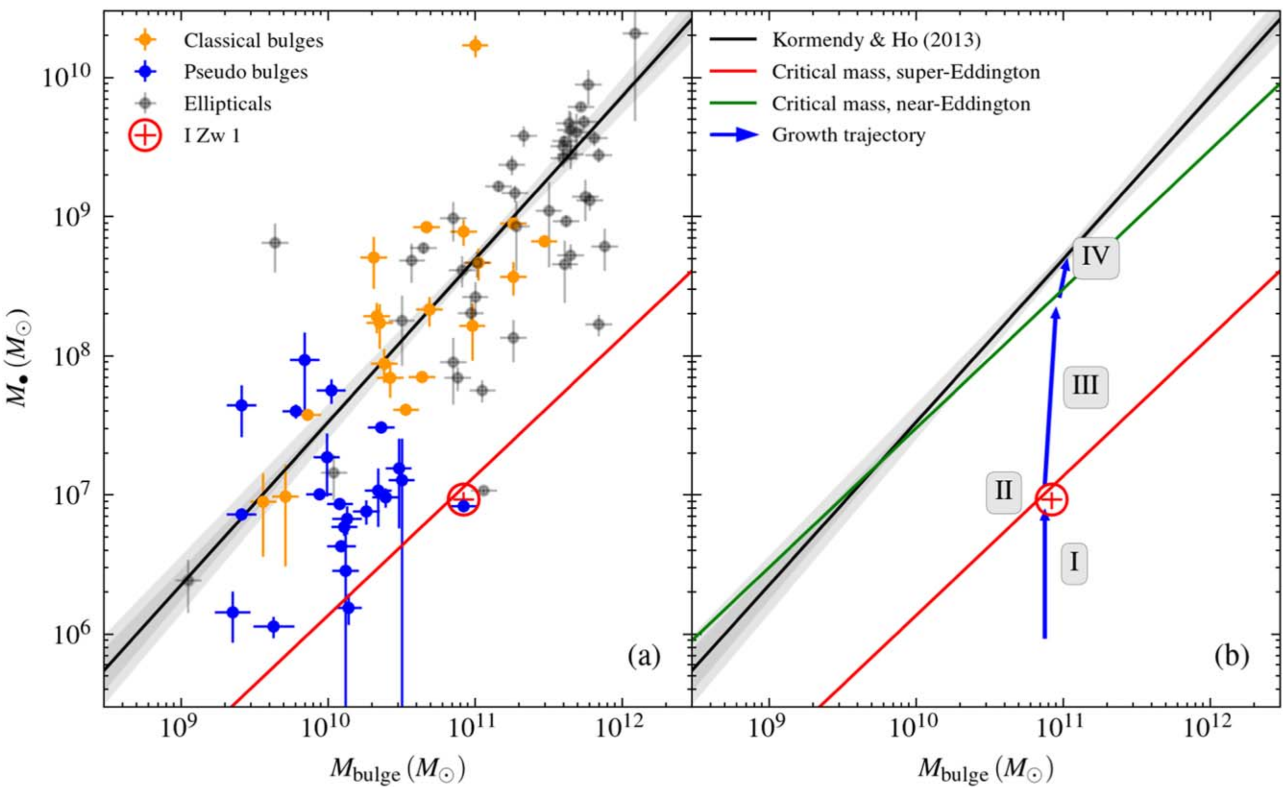

Figure 6. Panel (a): the correlation between BH mass ($M_\bullet$) and bulge stellar mass ($M_{\rm bulge}$). The data points are from Kormendy & Ho (2013), with the black line representing the best fit for elliptical and classical bulges. The BH and bulge mass for I Zw 1 (red point) are from Huang et al. (2019) and Zhao et al. (2021), respectively. I Zw 1 is a strong outlier. The red line is the $M_{\rm bulge}$-dependent critical mass relation for super-Eddington sources (Equation (12)) predicted by King & Muldrew (2016). Panel (b): the green curve shows the critical mass for near-Eddington sources (Equation (10); see also King & Pounds 2015), while the black and red curves are the same as in panel (a). The blue arrows show the inferred BH growth trajectory of I Zw 1, as discussed in Section 4.3. With different mass accretion rate, the trajectory can be summarized into four phases (I–IV). A schematic physical picture of the four phases of BH growth is shown in Figure 7.

with shocked gas; instead, they may have the same origin as IW 1, although they may not be generated in the same disk region. The corresponding post-shock gas locations for IW 2 and IW 3 support the physical picture proposed by King (2010a), which interprets WAs as the by-product of outflow shocks. The shocks produced by outflows may naturally produce thin layers of ionized gas (see also the last paragraph of Section 3). The strong variation of ionization state for IW 2 and IW 3 additionally suggests that they may have a large dispersion in density, which implies $b \ll 1$.

4.3. BH Mass and Feedback

Studying the mass of the BH in I Zw 1 in the context of the bulge properties of the host galaxy offers some insights into how the BH grows and the role of AGN feedback. I Zw 1 is a distinct outlier in the $M_\bullet$–$M_{\rm bulge}$ relation established by local, inactive galaxies (Figure 6).[13] With $M_\bullet = 9.3 \times 10^6\, M_\odot$ (Huang et al. 2019) and $M_{\rm bulge} = 10^{10.96\pm0.49}\, M_\odot$ (Zhao et al. 2021), I Zw 1 falls 1.4 dex below the $M_\bullet$–$M_{\rm bulge}$ relation of classical bulges and ellipticals (Kormendy & Ho 2013). Even if we admit the possibility that I Zw 1 might host a pseudo bulge instead of a classical bulge on account of its relatively low Sérsic (1963) index of $n = 1.69$ (Zhao et al. 2021),[14] its $M_\bullet$ still deviates by 1.2 dex from the zero-point of pseudo bulges (Li et al. 2022).

Why is I Zw 1 so offset below the nominal BH-bulge scaling relation? We suggest that the undermassive BH in I Zw 1 is a direct consequence of the momentum-driven outflow associated with its super-Eddington accretion. Several observational clues hint that the IWs of I Zw 1 have undergone efficient cooling. Section 4.2 argues that all the IWs may be generated during the same period of AGN activity and share a common origin. The data archives of XMM-Newton have recorded a total of 479 ks of observations of I Zw 1 spanning ∼20 yr, among which the highly ionized Fe XXV/XXVI absorber (IW 1) has been detected ∼80% of the time (Mizumoto et al. 2019 and this work). This suggests that highly ionized outflows may have been launched during a great fraction of the AGN's lifetime. This inference also applies to IW 2 and IW 3 because IWs are likely to be generated during the same AGN period (Section 4.2), and they both exist in epochs b and d. Yet, the IWs are localized to sub-parsec scales ($R_{\rm max} = 0.36$ pc for IW 1; Section 4.1). Nor do we detect significant large-scale outflows in molecular (CO emission; Cicone et al. 2014; Shangguan et al. 2020; Molina et al. 2021) or ionized (Hα emission; Molina et al. 2022) form. Although the observed ξ–v_w relation strongly links the winds to super-Eddington

[13] We focus on the $M_\bullet$–$M_{\rm bulge}$ relation instead of the $M_\bullet$–σ relation because we are not aware of any reliable stellar velocity dispersion measurements for the bulge of I Zw 1. Wang & Lu (2001) provide an estimate of $\sigma = 442$ km s^{-1} based on the width of the [O III] λ5007 emission line, but velocity dispersions derived from ionized gas can overestimate systematically the true stellar velocity, especially in luminous and high-Eddington ratio AGNs (Greene & Ho 2005; Ho 2009; Kong & Ho 2018).

[14] Gao et al. (2020) show that the Sérsic index is not a robust classifier of bulge type.

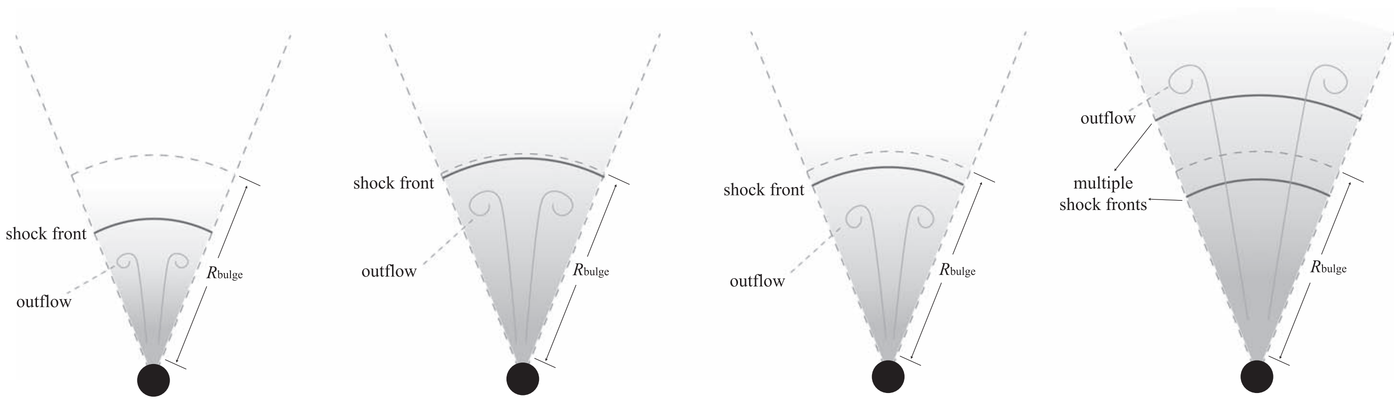

(I) $M_\bullet < M_c$, IWs are momentun-driven. Outflows cooled by ISM within the shock front, which is smaller than the bulge size. Gas inflow is not affected, allowing the BH to grow with high $\lambda_{\rm Edd}$.

(II) $M_\bullet \approx M_c$, IWs are momentun-driven. While the BH accumulates gas, outflows become increasingly powerful. A nearly critical mass BH allows the IWs to travel to bulge scales, suppressing the subsequent gas inflow and $\lambda_{\rm Edd}$.

(III) $M_\bullet \leq M_c$, IWs are momentun-driven. The reduced $\lambda_{\rm Edd}$ increases the critical mass, reducing the power of the outflows compared to phase II. The BH grows at the new $\lambda_{\rm Edd}$ and reaches the new $M_{c'}$. The continuous interplay between phase II and phase III finally leads to $M_c \to M_{c'}$ and $\lambda_{\rm Edd} \to 1$.

(IV) $M_\bullet \geq M_{c'}$, IWs are energy-driven. The BH finally attains a mass larger than the critical mass for near-Eddington accretion. Outflows become energy-driven, expand adiabatically, and produce large-scale molecular outflows that can expel the gas from the galaxy.

Figure 7. Cartoon showing the BH growth trajectory of I Zw 1. The black circle represents the central BH, launching gas outflows that interact with the host galaxy ISM (within the opening angle of the outflow). The specific energy of the outflow is color coded in gray. The evolution can be divided into four phases (Section 4.3): (I) when the super-Eddington BH is less massive than the critical mass ($M_\bullet < M_c$; Equation (12)), it will keep growing with negligible momentum-driven feedback; (II) as $M_\bullet \approx M_c$, the BH launches outflows with enough energy to limit the large-scale gas inflow; (III) the reduced $\lambda_{\rm Edd}$ elevates M_c, accretion resumes, as $\lambda_{\rm Edd} \to 1$ and $M_c \to M_c'$, the critical mass for near-Eddington source (Equation (10)); (IV) as accretion grows the BH, $M_\bullet \geqslant M_c'$, outflows become energy driven and finally halt the BH growth.

accretion, there is little evidence that the winds substantially affect the host galaxy on large scales.

In the context of quasar-mode AGN feedback (Fabian 2012), the BH affects its host galaxy by driving powerful outflows, injecting energy and momentum into its surroundings. The nature and effectiveness of the interaction between the outflow and the surrounding gas depend on the physics of the shocks. If the shocks cool efficiently, the wind is momentum driven, and only ram pressure is communicated to the ambient medium. Under these circumstances, it does not have enough energy to expel the gas because the thrust by the BH wind is too small to lift the weight of the swept-up gas shell against the gravitational potential of the galaxy bulge (King & Pounds 2015). By contrast, if the shocks do not cool, the wind is energy driven, and all of its energy is used to drive an adiabatically expanding bubble (King & Muldrew 2016), resulting in strong feedback effect.

According to the calculations of King & Pounds (2015), if the accretion rate is near-Eddington, the outflow remains momentum driven only if the BH mass is smaller than the critical value

$$M_c' = \frac{f_g \kappa}{\pi G^2}\sigma^4, \tag{10}$$

where $f_g = \Omega_{\rm baryon}/\Omega_{\rm matter} \approx 0.16$ is the gas fraction (Spergel et al. 2003), κ is the electron scattering opacity, G is the gravitational constant, and σ is the velocity dispersion of the bulge. This relation, which closely resembles the observed $M_\bullet - \sigma$ correlation (Ferrarese & Merritt 2000; Gebhardt et al. 2000; Kormendy & Ho 2013), suggests that feedback by outflows cuts off the growth of the BH at a mass close to this limiting value. The physical picture dramatically changes once $M_\bullet > M_c'$: the outflow quickly becomes energy driven, and the shocked wind can use all of its energy to push the interstellar gas as it expands into the bulge, which presumably suppresses further BH growth (King & Pounds 2015).

As discussed in Section 4.2, a super-Eddington outflow contains more momentum flux because it has higher optical depth. The critical BH mass is modified to (King & Muldrew 2016)

$$\begin{aligned} M_c &= \frac{\zeta'}{\zeta} M_c' = \frac{v_w}{2c\zeta\lambda_{\rm Edd}} M_c' \\ &\approx 3 \times 10^8 M_\odot \sigma_{200}^4 \frac{v_w}{2c\zeta\lambda_{\rm Edd}}, \end{aligned} \tag{11}$$

where Equations (7) and (9) have been used, and $\sigma_{200} = (\sigma/200\ {\rm km\,s^{-1}})$. As ζ is typically a constant of $\mathcal{O}(1)$ (King & Muldrew 2016), we expect $M_c \lesssim M_c'$. We can replace σ by $M_{\rm bulge}$ with the aid of the Faber & Jackson (1976) relation for galaxy spheroids, which in the V band is (Kormendy & Bender 2013)

$$L_V \approx 3.2 \times 10^{10} \sigma_{200}^4 L_{V,\odot}.$$

Based on the relation between color and mass-to-light ratio of Into & Portinari (2013) and the $B-I$ color of I Zw 1 (Zhao et al. 2021), we adopt $M/L_V = 2.7$, and Equation (11) transforms to

$$M_c \approx 3.5 \times 10^8 M_\odot \frac{M_{\rm bulge}}{10^{11} M_\odot} \frac{v_w}{2c\zeta\lambda_{\rm Edd}}. \tag{12}$$

Assuming $\zeta \simeq 0.5$ (Section 4.2) and a mean outflow velocity for IWs of $v_w \simeq 0.1c$ (Table 2), we plot Equation (12) as the red line in Figure 6. The prediction exactly matches the observed offset of I Zw 1 in the $M_\bullet - M_{\rm bulge}$ relation.

We suggest that the undermassive BH of I Zw 1 is the consequence of momentum-driven super-Eddington outflow feedback, which drives the bulge gas into an equilibrium state. Such a balance predicts that the BH growth of I Zw 1 should follow four phases (Figure 7), whose trajectory is schematically illustrated in Figure 6(b). I Zw 1 currently lies on the equilibrium line in which $M_\bullet \approx M_c$ (phase II). The dynamical equilibrium scenario guarantees that the growth process of the

BH produces a momentum-driven outflow, consistent with the evidence summarized above. This is because for a super-Eddington source, such as I Zw 1, the critical mass M_c scales inversely with $\lambda_{\rm Edd}$ (Equation (12)). This property ensures that the BH finally grows to a near-Eddington state (phase III). To understand the implication, we note that the feedback strength should correlate positively with the BH mass, as the feedback mechanism generally tends to maintain $M_\bullet \approx M_c$. At a given bulge stellar velocity dispersion σ or mass $M_{\rm bulge}$, once $M_\bullet \gtrsim M_c$ due to accretion, the outflow cooling efficiency declines, gas gets expelled from the nuclear region, and the central accretion event effectively extinguishes. The depletion in fuel reduces the luminosity of the AGN, and hence $\lambda_{\rm Edd}$, which then elevates the critical BH mass M_c. Now, $M_\bullet \lesssim M_c$, accretion is restarted, and the cycle repeats. In this manner the host galaxy gradually feeds the BH with decreasing rate, ultimately down to a near-Eddington value as the BH climbs toward the near-Eddington $M_\bullet - M_{\rm bulge}$ scaling relations (Equation (10); Figure 6(b)). Once $M_\bullet$ exceeds M_c', any outflow launched through accretion become energy driven. The gas will be gradually swept clear by the strong feedback, leaving only a very limited space for BH growth (phase IV).

The origin of the low-ionization UFOs also deserves attention. It is implausible to consider UFO 1 as the post-shock gas of IW 1 (Figure 5), as UFO 1 has slightly higher velocity but much lower ionization state than the highly ionized IW 1. The co-existence of outflows with very different ionization suggests that UFOs have a different origin than IWs. They could be associated with a more collimated outflow, in view of its high turbulence velocity, and thus presumably higher internal velocity dispersion. The low detection rate of such outflows may simply be the consequence of its much lower covering fraction, as evident by the high zero-point inferred from Figure 5 for the UFOs, which suggests $\Omega_{\rm IW} \gtrsim 50\,\Omega_{\rm UFO}$. Such a small covering factor indicates that UFOs impart a weak feedback effect on the host galaxy. As a consequence, we focus on the role of IWs when discussing the role of feedback in Figure 6.

4.4. Evolution of the X-Ray Corona

Previous studies suggest that the corona of I Zw 1 has a complicated structure, consisting of an extended component associated with the inner region of the accretion disk and a compact core collimated along the rotation axis of the BH that resembles the base of a jet-like structure (Wilkins et al. 2017, 2021). With the most recent measurement of $M_\bullet = 9.3 \times 10^6\,M_\odot$ from optical reverberation mapping (Huang et al. 2019), the characteristic light-crossing time[15] over the Schwarzschild radius is $R_{\rm S}/c = 2GM/c^3 = 91$ s. Over the lower frequency range, I Zw 1 exhibits an X-ray reverberation timescale of 160 s (Wilkins et al. 2017), which may reflect the reprocessing time lag due to the corona (for a review of X-ray reverberation, see Uttley et al. 2014). Considering that the measured reverberation lag can be diluted by up to ~75% due to the mixing of the reflection component and the continuum (Wilkins & Fabian 2012), the corona may extend up to about $3-4R_{\rm S}$ above the accretion disk, which corresponds to a timescale ~300 s Wilkins et al. (2017). With this in mind,

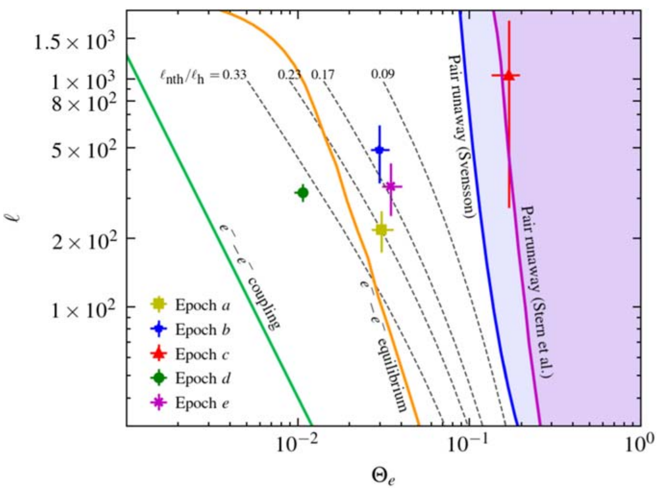

Figure 8. The variation of the corona temperature parameter Θ_e as a function of the compactness parameter ℓ. The time elapse for each epoch is ~20 hr. We show the theoretical predictions for pair runaway for a disk-like corona geometry (magenta curve; Stern et al. 1995) and for an isolated cloud (blue curve; Svensson 1984). Dotted lines represent calculations by Fabian et al. (2017) corresponding to different nonthermal fractions ℓ_{nth}/ℓ_h. We also mark the threshold for thermal $e^- - e^-$ coupling (green curve; Fabian 1994), beyond which cooling from electron interactions will dominate (orange curve; Ghisellini et al. 1993). Electrons in the region above the orange line do not have time to thermally equilibrate with each other before cooling occurs.

we take the characteristic size of the corona to be $R_{\rm corona} = 4R_{\rm S}$, which allows us to calculate the compactness parameter (Fabian et al. 2015)

$$\ell = \frac{L_{0.1-200}}{R_{\rm corona}} \frac{\sigma_{\rm T}}{m_e c^3},$$

with $L_{0.1-200}$ the 0.1−200 keV luminosity of the power-law component (Fabian et al. 2015), $\sigma_{\rm T}$ the Thomson cross section, and m_e the electron mass. To investigate what regulates the temperature of the plasma in the corona, we examine the relation between ℓ and the corona temperature parameter (Figure 8)

$$\Theta_e = \frac{kT_e}{m_e c^2}.$$

It has been proposed that the plasma temperature is maintained at the maximum value allowed by electron–positron pair production (Svensson 1984; Fabian et al. 2017). Ricci et al. 2018 showed that this behavior straightforwardly explains the observed positive correlation between the photon index and the Eddington ratio. During most of the observational epochs, I Zw 1 stayed well to the left of the pair runaway region of the $\ell - \Theta_e$ diagram (Figure 8), while in four out of the five epochs it lay beyond the electron-electron equilibrium line, which implies that the magnetic field could be important for stabilizing the hot corona because protons cannot supply the energy to the electrons fast enough, so the energy should be present there in some other form (Merloni & Fabian 2001; Fabian et al. 2015). Assuming that the corona is highly magnetized and powered by dissipation of magnetic energy, the values of the corona parameters can be explained by considering a compact plasma in which a fraction of the electrons are nonthermal (for the impact of such a hybrid corona, see Fabian et al. 2017). Figure 8 suggests that the

[15] Wilkins et al. (2017) used a different BH mass based on the single-epoch broad Hβ spectrum of I Zw 1(Vestergaard & Peterson 2006), which resulted in a significantly larger characteristic light-crossing time and thus a much smaller corona size in their analysis of the same data set (Wilkins et al. 2022).

nonthermal electron fraction of the corona of I Zw 1 may be ∼0.15–0.35.

The fluctuations between heating and cooling in our data show that the compact corona in I Zw 1 is likely to be a dynamic structure, with heating localized and highly intermittent in space and time (Fabian et al. 2015). The compactness parameter ℓ of the corona increased from ∼200 in epoch *a* to ∼500 in epoch *b* at an almost constant Θ_e. The corona was rapidly heated between epochs *b* and *c* surpassing the pair runaway threshold, which triggered significant cooling during epoch *d*, during which the temperature suddenly dropped from $\Theta_e \approx 0.2$ to 0.01. The state with the lowest temperature can be the most pair dominated because before annihilating the pairs can share the available energy, leading to a reduction in the mean energy per particle and thus the temperature of the thermal population, which may be composed mostly of pairs (Fabian et al. 2017). We note that Wilkins et al. (2022) only found a decrease of corona temperature between epochs *b* and *d*; they did not analyze the spectral property of I Zw 1 during epoch *c*.

5. Conclusions

We analyzed X-ray spectra of I Zw 1 observed simultaneously with XMM-Newton and NuSTAR in 2020 January. A major X-ray flare, together with several small peaks, were captured by the observations. The broadband (0.3−50 keV) spectrum, comprising a broad iron Kα line, a Compton hump at ∼25 keV, and a moderate soft excess below 1.0 keV, can be described well by a relativistic reflection model such as RELXILLCP. We detected two kinds of ionized absorbers with distinct ionization state and turbulence velocity. A prominent absorber, which we term IW 1, newly emerged from a momentum-driven outflow during the X-ray flare that occurred ∼216 ks (epoch *b*) into the NuSTAR observation. We use the long-duration, simultaneous NuSTAR and XMM-Newton observation to derive distances and other physical properties of the absorbing clouds.

The main conclusions are as follows:

1. The broadband X-ray continuum is dominated by a power law and can be described by the standard disk reflection model RELXILLCP after adding appropriate absorbers in the soft band. The best-fit results support a maximally spinning BH with $a_* > 0.973$, which is generally consistent with previous studies. The derived disk inclination angle $i = 42.3^{+2.4}_{-2.2}$ and iron abundance $A_{\rm Fe} = 3.51^{+0.37}_{-0.52}$ are slightly smaller than previous values (Section 3.1).
2. We detect five absorbers, two of them broad ($v_{\rm turb} \gtrsim 2500$ km s^{-1}) and the other three narrow ($v_{\rm turb} = 500$ km s^{-1}). We derived distances, energy rates, and momentum rates assuming that the outflows are either smooth or super-Eddington (Sections 3.2 and 4.1).
3. The observed relation between ionization parameter and outflow velocity for the dominant outflow follows a power-law relation of the form $\xi \sim v_w^{3.24}$ (Figure 5), as expected from a super-Eddington wind (Section 4.2).
4. The ionized winds in I Zw 1 are consistent with being momentum driven. The high outflow efficiency indicated by the super-Eddington nature of the winds would result in a lower equilibrium BH mass than expected compared with the given bulge properties of the host galaxy, consistent with the observed undermassive BH in I Zw 1 (Section 4.3; Figures 6 and 7).
5. In four out of five epochs, the continuum parameters of I Zw 1 on the $\ell - \Theta_e$ diagram lie beyond the electron-electron equilibrium line, suggesting that the magnetic field should be important in stabilizing hot corona, which has a nonthermal electron fraction of ∼0.15−0.35 (Section 4.4 and Figure 8).
6. The compact corona of I Zw 1 undergoes major fluctuations in heating and cooling, likely reflecting its dynamic structure, which experiences localized, highly intermittent heating that results in episodic pair runaway and cooling events (Section 4.4).

We thank the anonymous referee for helpful suggestions. This work was supported by the National Science Foundation of China (11721303, 11991052, 12011540375), the China Manned Space Project (CMS-CSST-2021-A04). C.R. acknowledges support from Fondecyt Iniciacion grant 11190831 and ANID BASAL project FB210003. All figures in this paper were produced with SCIENCEPLOTS (Garrett 2021).

ORCID iDs

Yuanze Ding https://orcid.org/0000-0002-5770-2666
Ruancun Li https://orcid.org/0000-0001-8496-4162
Luis C. Ho https://orcid.org/0000-0001-6947-5846
Claudio Ricci https://orcid.org/0000-0001-5231-2645

References

Abramowicz, M. A., Czerny, B., Lasota, J. P., & Szuszkiewicz, E. 1988, ApJ, 332, 646
Arnaud, K. A. 1996, in ASP Conf. Ser. 101, Astronomical Data Analysis Software and Systems V, ed. G. H. Jacoby & J. Barnes (San Francisco: ASP), 17
Blustin, A. J., Page, M. J., Fuerst, S. V., Branduardi-Raymont, G., & Ashton, C. E. 2005, A&A, 431, 111
Braito, V., Reeves, J. N., Matzeu, G. A., et al. 2018, MNRAS, 479, 3592
Brightman, M., Silverman, J. D., Mainieri, V., et al. 2013, MNRAS, 433, 2485
Bu, D.-F., & Yang, X.-H. 2021, ApJ, 921, 100
Cicone, C., Maiolino, R., Sturm, E., et al. 2014, A&A, 562, A21
Costantini, E., Gallo, L. C., Brandt, W. N., Fabian, A. C., & Boller, T. 2007, MNRAS, 378, 873
Czerny, B., Nikolajuk, M., Różańska, A., et al. 2003, A&A, 412, 317
Danehkar, A., Nowak, M. A., Lee, J. C., & Smith, R. K. 2017, PASP, 130, 024501
Dauser, T., Garcia, J., Parker, M. L., Fabian, A. C., & Wilms, J. 2014, MNRAS, 444, L100
Done, C., Davis, S. W., Jin, C., Blaes, O., & Ward, M. 2012, MNRAS, 420, 1848
Done, C., Sobolewska, M. A., Gierliński, M., & Schurch, N. J. 2007, MNRAS, 374, L15
Faber, S. M., & Jackson, R. E. 1976, ApJ, 204, 668
Fabian, A. C. 1994, ApJS, 92, 555
Fabian, A. C. 2012, ARA&A, 50, 455
Fabian, A. C., Lohfink, A., Belmont, R., Malzac, J., & Coppi, P. 2017, MNRAS, 467, 2566
Fabian, A. C., Lohfink, A., Kara, E., et al. 2015, MNRAS, 451, 4375
Fabian, A. C., Vaughan, S., Nandra, K., et al. 2002, MNRAS, 335, L1
Ferrarese, L., & Merritt, D. 2000, ApJL, 539, L9
Foreman-Mackey, D., Hogg, D. W., Lang, D., & Goodman, J. 2013, PASP, 125, 306
Gallo, L. C., Boller, T., Brandt, W. N., Fabian, A. C., & Vaughan, S. 2004, A&A, 417, 29
Gao, H., Ho, L. C., Barth, A. J., & Li, Z.-Y. 2020, ApJS, 247, 20
García, J., Dauser, T., Lohfink, A., et al. 2014, ApJ, 782, 76
García, J. A., Kara, E., Walton, D., et al. 2019, ApJ, 871, 88
Garrett, J. 2021, SciencePlots v1.0.9, Zenodo, doi:10.5281/zenodo. 4106649
Gebhardt, K., Bender, R., Bower, G., et al. 2000, ApJL, 539, L13

Ghisellini, G., Haardt, F., & Fabian, A. C. 1993, MNRAS, 263, L9
Gofford, J., Reeves, J. N., McLaughlin, D. E., et al. 2015, MNRAS, 451, 4169
Greene, J. E., & Ho, L. C. 2005, ApJ, 630, 122
Grevesse, N., Noels, A., & Sauval, A. J. 1996, in ASP Conf. Ser. 99, Cosmic Abundances, ed. S. S. Holt & G. Sonneborn (San Francisco, CA: ASP), 117
Haardt, F., & Maraschi, L. 1991, ApJL, 380, L51
Haardt, F., & Maraschi, L. 1993, ApJ, 413, 507
Harrison, F. A., Craig, W. W., Christensen, F. E., et al. 2013, ApJ, 770, 103
Hashizume, K., Ohsuga, K., Kawashima, T., & Tanaka, M. 2015, PASJ, 67, 58
Heckman, T. M., & Best, P. N. 2014, ARA&A, 52, 589
Ho, L. C. 2009, ApJ, 699, 638
Huang, Y.-K., Hu, C., Zhao, Y.-L., et al. 2019, ApJ, 876, 102
Into, T., & Portinari, L. 2013, MNRAS, 430, 2715
Jansen, F., Lumb, D., Altieri, B., et al. 2001, A&A, 365, L1
Jiang, Y.-F., Stone, J. M., & Davis, S. W. 2014, ApJ, 796, 106
Jiang, Y.-F., Stone, J. M., & Davis, S. W. 2019, ApJ, 880, 67
Kalberla, P. M. W., Burton, W. B., Hartmann, D., et al. 2005, A&A, 440, 775
Kallman, T., & Bautista, M. 2001, ApJS, 133, 221
King, A. 2003, ApJL, 596, L27
King, A. 2005, ApJL, 635, L121
King, A., & Muldrew, S. I. 2016, MNRAS, 455, 1211
King, A., & Pounds, K. 2015, ARA&A, 53, 115
King, A. R. 2010a, MNRAS, 402, 1516
King, A. R. 2010b, MNRAS, 408, L95
Kong, M., & Ho, L. C. 2018, ApJ, 859, 116
Kormendy, J., & Bender, R. 2013, ApJL, 769, L5
Kormendy, J., & Ho, L. C. 2013, ARA&A, 51, 511
Li, R., Ho, L. C., Ricci, C., et al. 2022, ApJ, submitted
Longinotti, A. L., Krongold, Y., Guainazzi, M., et al. 2015, ApJ, 813, L39
Martínez-Paredes, M., Aretxaga, I., Alonso-Herrero, A., et al. 2017, MNRAS, 468, 2
Merloni, A., & Fabian, A. C. 2001, MNRAS, 321, 549
Middleton, M. J., Walton, D. J., Roberts, T. P., & Heil, L. 2014, MNRAS, 438, L51
Mizumoto, M., Done, C., Tomaru, R., & Edwards, I. 2019, MNRAS, 489, 1152
Molina, J., Ho, L. C., Wang, R., et al. 2022, ApJ, submitted
Molina, J., Wang, R., Shangguan, J., et al. 2021, ApJ, 908, 231
Ohsuga, K., & Mineshige, S. 2011, ApJ, 736, 2
Ohsuga, K., & Mineshige, S. 2014, SSRv, 183, 353
Pinto, C., Alston, W., Parker, M. L., et al. 2018, MNRAS, 476, 1021
Pinto, C., Kaastra, J. S., Costantini, E., & de Vries, C. 2013, A&A, 551, A25
Piro, L., de Rosa, A., Matt, G., & Perola, G. C. 2005, A&A, 441, L13
Porquet, D., & Dubau, J. 2000, A&AS, 143, 495
Porquet, D., Reeves, J. N., O'Brien, P., & Brinkmann, W. 2004, A&A, 422, 85
Pounds, K. A., & King, A. R. 2013, MNRAS, 433, 1369
Pounds, K. A., Lobban, A., Reeves, J. N., Vaughan, S., & Costa, M. 2016, MNRAS, 459, 4389
Reeves, J. N., & Braito, V. 2019, ApJ, 884, 80
Reeves, J. N., Braito, V., Nardini, E., et al. 2016, ApJ, 824, 20
Ricci, C., Ho, L. C., Fabian, A. C., et al. 2018, MNRAS, 480, 1819
Ricci, C., Loewenstein, M., Kara, E., et al. 2021, ApJS, 255, 7
Risaliti, G., Young, M., & Elvis, M. 2009, ApJL, 700, L6
Sanfrutos, M., Longinotti, A. L., Krongold, Y., Guainazzi, M., & Panessa, F. 2018, ApJ, 868, 111
Serafinelli, R., Tombesi, Francesco, Vagnetti, Fausto, et al. 2019, A&A, 627, A121
Sérsic, J. L. 1963, BAAA, 6, 41
Shakura, N. I., & Sunyaev, R. A. 1973, A&A, 500, 33
Shangguan, J., Ho, L. C., Bauer, F. E., Wang, R., & Treister, E. 2020, ApJ, 899, 112
She, R., Ho, L. C., Feng, H., & Cui, C. 2018, ApJ, 859, 152
Shemmer, O., Brandt, W. N., Netzer, H., Maiolino, R., & Kaspi, S. 2008, ApJ, 682, 81
Silva, C. V., Costantini, E., Giustini, M., et al. 2018, MNRAS, 480, 2334
Sim, S. A., Long, K. S., Miller, L., & Turner, T. J. 2008, MNRAS, 388, 611
Spergel, D. N., Verde, L., Peiris, H. V., et al. 2003, ApJS, 148, 175
Springob, C. M., Haynes, M. P., Giovanelli, R., & Kent, B. R. 2005, ApJS, 160, 149
Steenbrugge, K. C., Fenovčík, M., Kaastra, J. S., Costantini, E., & Verbunt, F. 2009, A&A, 496, 107
Stern, B. E., Poutanen, J., Svensson, R., Sikora, M., & Begelman, M. C. 1995, ApJ, 449, L13
Svensson, R. 1984, MNRAS, 209, 175
Tombesi, E. 2016, AN, 337, 410
Tombesi, F., Cappi, M., Reeves, J. N., et al. 2010, A&A, 521, A57
Trakhtenbrot, B., Ricci, C., Koss, M. J., et al. 2017, MNRAS, 470, 800
Uttley, P., Cackett, E. M., Fabian, A. C., Kara, E., & Wilkins, D. R. 2014, A&ARv, 22, 72
Vestergaard, M., & Peterson, B. M. 2006, ApJ, 641, 689
Vignali, C., Iwasawa, K., Comastri, A., et al. 2015, A&A, 583, A141
Wang, T., & Lu, Y. 2001, A&A, 377, 52
Wilkins, D. R., & Fabian, A. C. 2012, MNRAS, 424, 1284
Wilkins, D. R., Gallo, L. C., Costantini, E., Brandt, W. N., & Blandford, R. D. 2021, Natur, 595, 657
Wilkins, D. R., Gallo, L. C., Costantini, E., Brandt, W. N., & Blandford, R. D. 2022, MNRAS, 512, 761
Wilkins, D. R., Gallo, L. C., Silva, C. V., et al. 2017, MNRAS, 471, 4436
Wilms, J., Allen, A., & McCray, R. 2000, ApJ, 542, 914
Xu, Y., García, J. A., Walton, D. J., et al. 2021, ApJ, 913, 13
Yang, Q.-X., Xie, F.-G., Yuan, F., et al. 2015, MNRAS, 447, 1692
Zhao, Y., Ho, L. C., Shangguan, J., et al. 2021, ApJ, 911, 94
Zubovas, K., & King, A. R. 2014, MNRAS, 439, 400